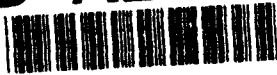


AD-A250 028



TION PAGE

Form Approved
OMB No. 0704-0188

average 1 hour per response, including the time for reviewing instructions, searching existing data sources, the collection of information. Send comments regarding this burden estimate or any other aspect of this Washington Headquarters Services, Directorate for Information Operations and Reports, 1215 Jefferson Avenue, Suite 1010, Office of Management and Budget, Paperwork Reduction Project (0704-0188), Washington, DC 20503.

1. AGENCY USE ONLY (Leave blank)		2. REPORT DATE 4/13/92		3. REPORT TYPE AND DATES COVERED Annual Technical 15 April 1991	
4. TITLE AND SUBTITLE Laser Material Interactions				5. FUNDING NUMBERS AFOSR-89-0337	
6. AUTHOR(S) Professor S.R.J. Brueck					
7. PERFORMING ORGANIZATION NAME(S) AND ADDRESS(ES) Center for High Technology Materials University of New Mexico Electrical & Computer Engineering Building, Room 125 Albuquerque, NM 87131-6081				8. PERFORMING ORGANIZATION REPORT NUMBER AFOSR-TR- 02 0312	
9. SPONSORING/MONITORING AGENCY NAME(S) AND ADDRESS(ES) AFOSR/NE Bldg. 410 Bolling AFB, DC 20332				10. SPONSORING/MONITORING AGENCY REPORT NUMBER 2301/AS	
11. SUPPLEMENTARY NOTES					
12a. DISTRIBUTION/AVAILABILITY STATEMENT unlimited				12b. DISTRIBUTION CODE DTIC ELECTE MAY 14 1992 S D D	
13. ABSTRACT (Maximum 200 words) The Laser-Materials Interaction Laboratory at the Center for High Technology Materials at the University of New Mexico, which is devoted to a broad range of laser spectroscopic probes of semiconductor and nonlinear materials, fabrication processes, and optoelectronic devices, carries out much of this work in conjunction with the Optoelectronics Research Center Program, also funded by AFOSR. During the period of this report significant progress was made in a number of areas, including ultrafast operation of optically-pumped resonant periodic-gain GaAs surface-emitting lasers, grating coupling to surface-plasma waves, and high-speed Si Schottky photodiodes.					
<div style="border: 1px solid black; padding: 5px; width: fit-content;"> This document has been approved for public release and sale; its distribution is unlimited. </div>					
14. SUBJECT TERMS				15. NUMBER OF PAGES 35 plus cover	
				16. PRICE CODE	
17. SECURITY CLASSIFICATION OF REPORT Unclassified	18. SECURITY CLASSIFICATION OF THIS PAGE Unclassified	19. SECURITY CLASSIFICATION OF ABSTRACT Unclassified	20. LIMITATION OF ABSTRACT		

LASER-MATERIAL INTERACTIONS

Professor S.R.J. Brueck
Center for High Technology Materials
University of New Mexico
Albuquerque, NM 87031-6081

13 April 1992

Technical Report for Period 16 April 1990 - 15 April 1991

Prepared for

Department of the Air Force
Air Force Office of Scientific Research
Building 410
Bolling Air Force Base, DC 20332-6448

Office of Naval Research
Bandelier West
University of New Mexico
Albuquerque, NM 87131

Accession For	
NTIS CRA&I	<input checked="" type="checkbox"/>
DTIC TAB	<input type="checkbox"/>
Unannounced	<input type="checkbox"/>
Justification	
By	
Distribution /	
Availability Codes	
Dist	Avail and/or Special
A-1	



92-12612



92 5 11 084

Introduction:

The Laser-Materials Interaction Laboratory at the Center for High Technology Materials of the University of New Mexico is devoted to the study of a broad range of laser spectroscopic probes of semiconductor and nonlinear materials, fabrication processes and optoelectronic devices. Much of this work is being carried out in conjunction with the Optoelectronics Research Center Program at CHTM, which is also partially funded by the Air Force Office of Scientific Research. Significant progress has been made during this reporting period in a number of areas including: ultrafast operation of optically-pumped resonant periodic-gain GaAs surface-emitting lasers; grating coupling to surface-plasma waves; and high-speed Si Schottky photodiodes. Only brief summaries of this work are presented here. More detailed descriptions are included in the attached preprints and reprints.

Ultrafast operation of RPG-VCSELs:

High speed pulsed operation of surface-emitting lasers is necessary for applications involving information processing. We have investigated experimentally and theoretically the picosecond dynamics of resonant periodic gain (RPG) vertical cavity surface emitting lasers (VCSEL) optically pumped directly into the gain region. The pulsewidths and pulseshapes obtained from the cross correlation of pump and signal pulses, showed a fast rise and a relatively slower fall time. This was the first report of time-resolved output pulse shapes for these lasers. The shortest pulse width of ~ 13.4 ps obtained at a pump fluence ($\sim 5 \times$ threshold) of 0.6 nJ. The dependence of pulseshape and pulse delay agree well with a simple rate equation gain switching model. This model gives a cavity lifetime of 8.3 ps and, thus, a lower bound on the cavity mirror reflectivities of $R_1 R_2 > 0.99$. This is the first direct measurement of the mirror reflectivities and is in good agreement with the values calculated from simple Fresnel reflectivity models.

Grating Coupling to Surface-Plasma Waves:

Work on this project was primarily completed and reported in the prior annual report. Papers based on this work have now been published and are included in the appendix.

High-Speed Si Schottky Photodiodes:

Relatively little work has been reported on high-speed ultraviolet detectors. As ultrafast UV-sources become more available, there is increasing interest in high-speed detectors for monitoring photochemical and other high-speed phenomena. In addition, UV is always of interest for space-based systems because of the reduced optics size associated with the shorter wavelength.

Application will require development of improved detectors as well as sources. We have developed and tested (UV-heterodyne characterization at 334 nm) high-speed planar Ni-Si-Ni Schottky barrier photodetectors. For a 4.5- μm gap geometry, a 16-GHz 3-dB heterodyne response, limited by packaging effects, is measured at a wavelength of 334 nm. This is the highest reported speed for a Si detector at any wavelength. A photodiode transport model, including carrier drift, diffusion, and recombination is in good agreement with the measured detector frequency response. This model gives a 24-GHz 3-dB point for the present detector exclusive of packaging response and predict a 86-GHz 3-dB response for a 1- μm gap geometry.

Laser-Material Interactions

PUBLICATIONS

A cumulative list of publications for this program is attached. Only new manuscripts or newly published versions of previously reported preprints are included in the appendix. These are printed in **boldface** in the publications list.

S. R. J. Brueck, A. Mukherjee and A. Y. Wu

Nonlinear Optics of Thin-Film PLZT

Proceedings of the 12th International Vavilov Conference on Nonlinear Optics

R. C. Dye, R. E. Muenchausen, N. S. Nogar, A. Mukherjee and S. R. J. Brueck

Laser Writing of Superconducting Patterns on YBa₂Cu₃O_x Films

Appl. Phys. Lett. **57**, 1149-1151 (1990).

D. L. McDaniel, J. G. McInerney, M. Y. A. Raja. C. F. Schaus, and S. R. J. Brueck

Vertical Cavity Surface-Emitting Laser with CW Injection Laser Pumping
Photonics Tech. Lett. **2**, 156-158 (1990)

M. Mahbobzadeh, M. Y. A. Raja, J. G. McInerney, C. F. Schaus and S. R. J. Brueck

Mode Stability and Spectral Properties of Resonant Periodic Gain Surface-Emitting Lasers

SPIE 1219 Laser Diode Technology and Applications II, D. Botez and L. Figueroa, eds. 264-275 (1990).

R. E. Muenchausen, R. C. Dye, R. C. Estler, S. Folytn, A. R. Garcia, K. M. Hubbard, N. S. Nogar, X. D. Wu, A. Carim, A. Mukherjee and S. R. J. Brueck
Pulsed Laser Processing of High Temperature Superconducting Thin Films
Proceedings 4th SAMPE International Conference.

A. Mukherjee, S. R. J. Brueck and A. Y. Wu

Electric-Field Induced Second Harmonic Generation in PLZT

Opt. Commun. **76**, 220-222 (1990)

A. Mukherjee, S. R. J. Brueck and A. Y. Wu

Electro-Optic Effects in Thin-Film Lanthanum-Doped Lead Zirconate Titanate

Optics Lett. **15**, 151-153 (1990)

A. Mukherjee, M. Mahbobzadeh, C. F. Schaus and S. R. J. Brueck
Ultrafast Operation of Optically Pumped Resonant Periodic Gain
GaAs Surace Emitting Lasers

Photonics Tech. Lett. **2**, 857-859 (1990).

B. W. Mullins, S. F. Soares, K. A. McArdle, C. M. Wilson and S. R. J. Brueck

A Simple High-Speed Si Schottky Photodiode
Photonics Tech. Lett. 3, 360-362 (1991).

M. Y. A. Raja, D. W. Reicher, S. R. J. Brueck and J. R. McNeil
High Sensitivity Surface-Photoacoustic Spectroscopy
Optics Lett. 15, 66-68 (1990)

Saleem H. Zaidi, M. Yousaf, and S. R. J. Brueck
Grating Coupling to Surface Plasma Waves I - First-Order Coupling
Jour. Opt. Soc. Amer. B8, 770-779 (1991)

Saleem H. Zaidi, M. Yousaf, and S. R. J. Brueck
Grating Coupling to Surface Plasma Waves II - Interactions between
First and Second-Order Coupling
Jour. Opt. Soc. Amer. B8, 1348-1359 (1991)

Saleem Zaidi, M. Yousaf and S. R. J. Brueck
Characterization of Thin Al Films using Grating Coupling to Surface Plasma
Waves
submitted to Journal of Applied Physics

**Ultrafast Operation of Optically Pumped
Resonant Periodic Gain GaAs Surface
Emitting Lasers**

**A. Mukherjee
M. Mahbobzadeh
C. F. Schaus
S. R. J. Brueck**

**Reprinted from
IEEE PHOTONICS TECHNOLOGY LETTERS
Vol. 2, No. 12, December 1990**

Ultrafast Operation of Optically Pumped Resonant Periodic Gain GaAs Surface Emitting Lasers

A. MUKHERJEE, M. MAHBOBZADEH, C. F. SCHAUS, AND S. R. J. BRUECK

Abstract—Generation and characterization of picosecond optical pulses from vertical-cavity resonant-periodic-gain GaAs-AlGaAs surface-emitting lasers optically pumped by picosecond dye-laser pulses is reported. The output pulseshape was obtained from the cross correlation of pump and signal pulses. Dependence of signal pulsewidth and pulse delay on pump power were investigated. The results are in good agreement with a simple rate equation model of the pulse formation. A cavity lifetime of 8.3 ps, compared with a gain medium transit time of ~ 0.1 ps, is determined for this very high- Q structure.

I. INTRODUCTION

INTEREST in vertical-cavity surface-emitting lasers (VCSEL's) has grown recently. The rapid progress has been due largely to the development of high-reflectivity Bragg reflectors which are grown (by either MOCVD or MBE) as an integral part of the laser structure. The relative simplicity of fabrication, the potential for low threshold, high efficiency lasers, and for high density two-dimensional array operation are especially attractive. Several alternate configurations of the gain region including simple heterostructures [1], multiple quantum wells [2], resonant periodic gain (RPG) multiple quantum wells [3], ($\lambda/2$ separation), and single quantum well [4], have been demonstrated with either electrical or optical excitation.

For applications involving information processing, high-speed pulsed operation of these lasers is necessary. The very short cavity length (~ 2 – 5 μm) results in a very rapid photon transit time; however, the very high- Q resonators necessary for laser operation substantially lengthen the cavity lifetime, and hence the gain-switched pulsewidth. Optical pumping with ultrafast laser pulses provides an important technique for evaluating the fundamental laser temporal behavior without the complications of circuit parasitics which inevitably effect electrical pumping measurements. A modulation bandwidth of 8 GHz has been reported by Jewell *et al.* [5]. Raja *et al.* [6] reported optical pumping results for a 20-period RPG GaAs-GaAlAs laser excited at 620 nm where the dominant

excitation was into the first Bragg reflector followed by photoluminescence pumping of the gain region. Time delays between the pump pulse and the RPG output were ~ 1 ns dominated by the photoluminescence lifetime; instrumentation-limited pulse width measurements were ~ 1 ns. Recently, Karin *et al.* [7] reported on autocorrelation measurements for an optically-pumped MBE-grown 20-period RPG VCSEL with 30-nm quantum wells. Pulsewidths of < 6 ps were reported for a comparatively low- Q cavity (92.2 and 98% mirror reflectivities).

In this letter, we report on experimental observation and theoretical simulation of the picosecond dynamics of RPG VCSEL's optically pumped directly into the gain region. The pulsewidths and pulseshapes obtained from the cross correlation of pump and signal pulses, showed a fast rise and a relatively slower fall times. This is the first report of time-resolved output pulse shapes for these lasers. The shortest pulsewidth of ~ 13.4 ps was obtained at a pump fluence (approximately five times threshold) of ~ 0.6 nJ (4-ps pump pulsewidth in a ~ 10 - μ diameter spot). This same structure was previously used for CW investigations [3] and had very high calculated mirror reflectivities ($R_1 R_2 \sim 99.6\%$). The dependence of the output pulsewidth and delay on the pump power are reported. The pulsewidth, pulseshape, and delay agree well with a simple rate equation model.

II. THEORY

The normalized rate equations describing the temporal behavior of the carrier density and the optical intensity in the laser cavity are given by

$$\frac{dn}{d\tau} = -n \left(\frac{\tau_c}{\tau_g} \right) - S(n - n_c) + P \left(\frac{\tau_c}{\tau_g} \right) \quad (1)$$

$$\frac{dS}{d\tau} = -S + S(n - n_c) \quad (2)$$

where

τ = time normalized to the cavity lifetime ($= t/\tau_c$)

n = carrier density (normalized to the clamped carrier density above threshold, neglecting transparency, $n_c = 1/\beta\tau_c$ where β is the gain coefficient per carrier)

S = photon density (also normalized to n_c)

P = optical pumping rate (normalized to the cw threshold, neglecting transparency requirements, $P_{th} = 1/\beta\tau_c\tau_g$)

τ_g = carrier lifetime in the gain region

τ_c = cavity lifetime, and

Manuscript received August 22, 1990; revised October 1, 1990. This work was supported by the Air Force Office of Scientific Research.

A. Mukherjee, M. Mahbobzadeh, and C. F. Schaus are with the Center for High Technology Materials and the Department of Electrical and Computer Engineering, University of New Mexico, Albuquerque, NM 87131.

S. R. J. Brueck is with the Center for High Technology Materials and the Department of Electrical and Computer Engineering and the Department of Physics and Astronomy, University of New Mexico, Albuquerque, NM 87131.

IEEE Log Number 9041164.

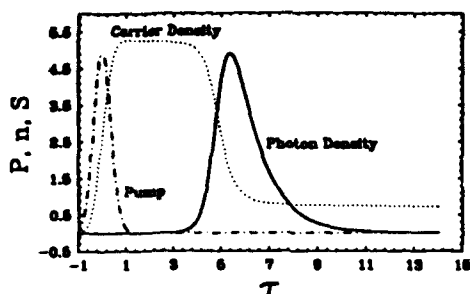


Fig. 1. Time evolution of pump pulse, carrier population and photon output based on a simple rate equation model of a gain-switched semiconductor laser.

n_g = the carrier concentration (normalized to n_c) required for transparency.

For a pump pulse with a Gaussian temporal profile of FWHM ~ 4 ps, (1) and (2) were numerically integrated using a simple predictor-corrector algorithm. The result for the temporal evolution of the carrier and photon density corresponding to a pump power of $5 P_{th}$ is shown in Fig. 1. The time scale is normalized to the cavity lifetime and the vertical axis to n_c . The pump pulse is also shown in this figure. Notice that the carrier density rises as the integral of the pump pulse and then undergoes a very slow spontaneous-emission decay while the photon density is building up from very low initial levels. The gain switched output pulse, along with a concomitant rapid depletion of the carrier density occurs after a delay of several cavity lifetimes. Note that the output pulse is asymmetrical with a relatively fast rise and a slower decay. Following the output pulse, the carrier concentration is depleted to below threshold and decays with the spontaneous lifetime. This model, neglecting gain and absorption saturation, Auger recombination, etc. is a simplification of the actual situation. However, it provides a very good fit to the experimental data. A simple model extension to empirically include gain saturation has been presented by Morton *et al.* [9].

III. EXPERIMENT

The VCSEL structure was grown by MOCVD on a GaAs substrate. The laser structure consisted of a $30\frac{1}{2}$ -period $Ga_{0.75}Al_{0.25}As$ -AlAs $\lambda/4$ -reflector stack (calculated reflectivity 99.9%), a 20-period RPG region with 10-nm GaAs quantum wells and $Ga_{0.8}Al_{0.2}As$ $\lambda/2$ -spacers, and a 20-period $Ga_{0.75}Al_{0.25}As$ -AlAs $\lambda/4$ -output reflector (calculated reflectivity 99.7%). The Al concentration in the gain region spacers was lower than that in the mirror stacks to allow for direct optical pumping of the gain region. Details of the MOCVD growth and laser structure have been reported previously [3].

The VCSEL was optically pumped with the output of a CW-modelocked dye laser (4-ps pulses, 82-MHz repetition rate at 740 nm). A typical second-harmonic intensity autocorrelation of the pump pulses showing an actual pulsewidth ~ 4 ps is shown at the inset in Fig. 2. Notice the absence of any coherence spike in the autocorrelation indicating stable dye-laser operation [8]. This pulse train was focused to a spot diameter of ~ 10 μm using a $10\times$ -microscope objective (available average power at the gain region was 60 mW accounting for optic loss, measured reflectivity from the VCSEL front surface and estimated absorption in the top

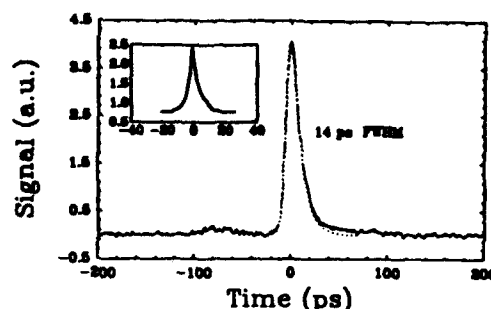


Fig. 2. Cross-correlation between the RPG VCSEL output pulse and the dye laser pump pulse for a pumping level approximately five times threshold. Note the asymmetry of the output pulse (solid line) in good agreement with the calculated pulse shape (dotted line). The theoretical time delay as well as the output level were arbitrarily adjusted for this fit. The insert shows the auto correlation of the pump pulse of ~ 4 ps FWHM.

mirror (15%); the VCSEL output was collected by the same objective and directed into the correlator along with a split-off portion of the pump-pulse train. The harmonic crystal was rotated to provide a cross-correlation response at the 398-nm sum frequency of the 740-nm pump and the 862-nm VCSEL output. This procedure provides the pulse width and a relative pulse delay. For the shortest pulse delay, both the pump pulse reflected from the VCSEL and the output pulse were observed with a fast detector and oscilloscope combination to provide a calibration of the peak-to-peak time delay (~ 16 GHz bandwidth to determine the absolute delay); this introduces a relative error of $\sim \pm 3$ ps.

The cross-correlation signal for the shortest VCSEL output observed is shown in Fig. 2. The pulse width is ~ 14 ps with a fast rise- and a relatively slower fall-time. Taking the finite pump pulsewidth into account, the pulsewidth of the VCSEL was estimated to be ~ 13.4 ps. The small prepulse is due to a residual satellite pulse present in the pump pulse train used for this particular measurement. The relatively longer pulsewidth from our VCSEL compared with a FWHM < 6 ps reported in [7] is attributed to our higher mirror reflectivities, resulting in longer cavity lifetimes. The dotted line is the numerical result from the rate equations for the parameters, $\tau_c = 8.3$ ps, $n_g = 0.5$, $\tau_s = 200 \tau_c$, and $P = 5$. The time delay and pulse amplitude were independently adjusted to match the experimental result. Good qualitative agreement with the details of the experimental pulseshape is obtained.

An input-output curve for the ultrafast operation, Fig. 3, of this VCSEL showed a threshold of 10-mW average power. The external slope efficiency of the theoretical input-output curve was adjusted to the experimental value of $\sim 10\%$. The cross-correlation data showing the pulsewidth and peak-to-peak delay as a function of pump power is shown in Fig. 3. The x-axis is pump power in units of threshold power and the y-axis is time in units of cavity lifetime. The solid lines represent the theoretical fit for the identical parameters used to fit the pulseshape (Fig. 2). In fitting these data, the calculated results for P were renormalized by $1/(1 + n_g)$ to account for the transparency requirements. That is, the definition of P_{th} neglects transparency requirements; since the experimental data are normalized to the actual threshold, including transparency requirements, the model values of P are divided by $(1 + n_g)$ for comparison. Again, there is very good agreement. There exists some uncertainty in the τ_s and

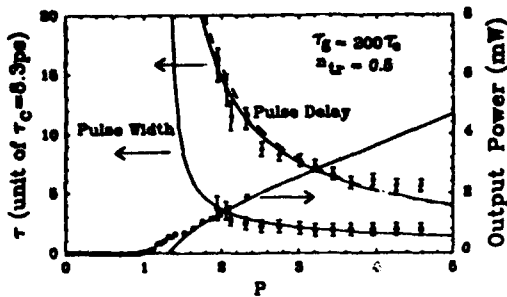


Fig. 3. Power dependence of the RPG VCSEL output pulsewidth, delay from the pump pulse, and output power. The power axis has been normalized to the observed threshold power for the experimental results and to the cw threshold (including transparency requirements) for the model results. Good agreement is obtained for a cavity lifetime of 8.3 ps. The dashed curve associated with the pulse delay data is an approximate analytic result (see text).

n_u values; comparable fits were obtained for a relatively wide range of values. A time-resolved photoluminescence experiment to independently measure τ_s is planned; this will allow a more precise estimate of n_u from this model. The experimental points for both pulsewidth and delay deviate from the theoretical fit towards longer times for higher pump powers. This may result from gain saturation or spectral hole burning leading to absorption saturation of the pump. Any mechanism that decreases the gain below the linear regime of the model will result in a saturation in the pulsewidth and delay above that predicted by this simple model.

IV. DISCUSSION

It is informative to compare the cavity lifetime with a simple cavity transit time. The cavity consists of the 20 $\lambda/2$ periods of the gain region plus the distributed mirror layers. An effective cavity length is given by including the mirror $1/e$ lengths ($\sim 10 \lambda/4$ sections for each mirror) along the gain region; this gives round-trip transit time τ_t of $\sim 9 \times 10^{-14}$ s. The effective cavity parameters are related to these times by the simple relationship

$$1 - R_1 R_2 e^{-2\alpha l} = \tau_t / \tau_c \quad (3)$$

where R_1 and R_2 are the mirror reflectivities and α is the (effective) loss coefficient due to background and mirror scattering and free carrier absorption. Assuming that the mirror reflectivities are the theoretical values of 99.9% and 99.7% for the present structure, (3) can be used to estimate $e^{-2\alpha l} \sim 0.993$. This result is consistent with the observed differential quantum efficiency in this experiment of $\sim 12\%$, but is inconsistent with the much higher differential (and indeed overall) power conversion efficiencies observed for CW excitation in this same structure [3]. This discrepancy may be due to higher photon losses in the pulse excitation case where much higher intensities leading to saturation and multiphoton excitation processes are possible. Detailed measurements as a function of mirror reflectivity are underway to resolve this issue.

It is possible to obtain an approximate analytic result for the time delay between the excitation and output pulses, assuming that both pulses are short compared with the time delay from (1) and (2). During this time delay, the photon density is negligible so that (1) simply gives an exponential decay for the carrier density from the initial excitation pulse

at the carrier lifetime τ_s . This result is then substituted back into (2) which can be integrated to yield

$$S(\tau) = S_0 \exp \left\{ -\tau(1 + n_u) + E(\tau_s/\tau_c)(1 - e^{-\tau/\tau_s}) \right\} \quad (4)$$

for a delay time much less than τ_s . Here, E is the integrated energy in the pump pulse. The second exponential in (4) can be expanded with the result that for an exponential growth of A for lasing the very simple result

$$\tau_{\text{delay}} \sim A\tau_c / [P - (1 + n_u)] \quad (5)$$

is obtained. Traditionally, values of A between 20 and 30 have been invoked for amplification above the background levels, a value of 23.5 provides the best fit with the detailed numerical calculation. This result is plotted as the dashed curve in Fig. 3. Good agreement is obtained with the more exact numerical calculation.

We have reported generation and characterization of ultrafast optical pulses from a GaAs-GaAlAs RPG VCSEL optically pumped by 4-ps duration dye-laser pulses. Cross-correlation experiments yield a minimum pulsewidth of ~ 13.4 ps as well as the asymmetric pulse shape, and the power dependence of the pulse duration and delay. These results are in good agreement with a simple rate equation model of the gain-switched pulses. Analysis of the results point to variations in cavity losses between CW and pulsed operation of these lasers. Clearly, a shorter cavity length and/or lower mirror reflectivities will yield shorter pulses. Further investigations are underway.

ACKNOWLEDGMENT

We wish to thank M. Y. A. Raja and A.-S. Chu for extensive assistance at the early stages of this investigation and J. G. McInerney and N. Mukherjee for many helpful discussions.

REFERENCES

- [1] K. Iga, F. Koyama, and S. Kinoshita, "Surface emitting semiconductor lasers," *IEEE J. Quantum Electron.*, vol. QE-24, 1845-1855, 1988.
- [2] Y. H. Wang, K. Tai, J. D. Wynn, M. Hong, R. J. Fisher, J. P. Mannaerts, and A. Y. Cho, "GaAs/AlGaAs multiple quantum well GRIN-SCH vertical cavity surface emitting laser diodes," *IEEE Photon. Technol. Lett.*, 2, pp. 456-458, 1990.
- [3] C. F. Schaus, M. Y. A. Raja, J. G. McInerney, H. E. Schaus, S. Sun, M. Mahbobzadeh, and S. R. J. Brueck, "High-efficiency CW operation of MOCVD-grown GaAs/AlGaAs vertical-cavity lasers with resonant periodic gain," *Electron. Lett.*, vol. 25, pp. 637-638, 1989.
- [4] Y. H. Lee, J. L. Jewell, A. Scherer, S. L. McCall, J. P. Harbison, and L. T. Florez, "Room temperature continuous-wave vertical cavity single-quantum-well microlaser/diodes," *Electron. Lett.*, vol. 25, p. 1377, 1989.
- [5] J. L. Jewell, Y. H. Lee, A. Scherer, S. L. McCall, N. A. Olsson, J. P. Harbison, and L. T. Florez, "Surface-emitting microlasers for photonic switching and interchip connections," *Opt. Eng.*, vol. 29, no. 3, pp. 210-212, 1990.
- [6] M. Y. A. Raja, A. Mukherjee, M. A. Mahbobzadeh, C. F. Schaus, and S. R. J. Brueck, *Conf. Dig. 1989 LEOS Ann. Meet.*, paper OE 11.5.
- [7] J. R. Karin, L. E. Melcer, J. E. Bowers, S. W. Corzine, R. S. Geels, and L. A. Coldren, *Conf. Dig. CLEO'90*, paper CFC2.
- [8] J.-C. Diels in *Femtosecond Dye Lasers: Principles and Applications*, F. Duarte and L. Hillman, Eds. Boston, MA: Academic, 1990.
- [9] P. A. Morton, D. L. Crawford, and J. E. Bowers, "Design of 1.3- μ m GaInAsP surface-emitting lasers for high-bandwidth operation," *Opt. Lett.*, vol. 15, pp. 679-681, 1990.

A Simple High-Speed Si Schottky Photodiode

B. W. Mullins, S. F. Soares, K. A. McArdle, C. M. Wilson, and S. R. J. Brueck

Abstract—Design, fabrication, and UV-heterodyne characterization of Ni-Si-Ni metal-semiconductor-metal Schottky barrier photodetectors is reported. Planar detectors were fabricated, with a simple 3-level lithography process on bulk Si, in both simple-gap and interdigitated geometries with gap dimensions from 1 to 5 μm . Frequency response of these devices was characterized using a CW-laser heterodyne system at 334.5 nm. For a 4.5- μm interdigitated device, a 3-dB response of 16 GHz is measured, giving 22 GHz when deconvolved from the package/connector. A detailed theoretical model of the photodiode response incorporating effects of carrier transport and device geometry is in excellent agreement with the measurement. This model predicts an 86-GHz 3-dB response for the 1- μm gap geometry devices.

INTRODUCTION

THERE has been extensive research on high-speed low-noise photodetectors in the 0.8–1.5 μm wavelength range for use in optical communication systems. Four general device designs, p-i-n [1], [2], vertical Schottky barrier [3], planar Schottky barrier [4]–[7], and avalanche photodiode [8], have been developed. Device materials include Si [5], [9], InGaAs [8], and strained-layer superlattices [10]. In the near infrared region, very fast, highly responsive detectors have been fabricated. Frequency responses up to 67 GHz and quantum efficiencies of 80% have been reported for p-i-n devices [2]. The fastest Schottky-barrier devices reported have a 110-GHz frequency response [4].

In contrast, relatively little work has been reported on ultraviolet detectors. As ultrafast UV sources become available, there is increasing interest in high-speed detectors for monitoring photochemical and other high-speed phenomena.

The most salient materials characteristic at UV wavelengths that determines detector design is the very high absorption coefficient of $\sim 10^6 \text{ cm}^{-1}$ for almost all semiconductors. This dictates a design with very shallow junctions in traditional vertical geometries and favors the planar structure.

Manuscript received October 31, 1990; revised January 15, 1991. This work was supported in part by the Naval Research Laboratory.

B. W. Mullins was with the Center for High Technology Materials and the Department of Physics and Astronomy, University of New Mexico, Albuquerque, NM. He is now with Phillips Laboratory, Kirtland Air Force Base, Albuquerque, NM 87117.

S. F. Soares is with the Center for High Technology Materials and the Department of Electrical and Computer Engineering, University of New Mexico, Albuquerque, NM 87131.

K. A. McArdle and C. M. Wilson are with the Center for High Technology Materials and the Department of Physics and Astronomy, University of New Mexico, Albuquerque, NM 87131.

S. R. J. Brueck is with the Center for High Technology Materials, the Department of Physics and Astronomy, and the Department of Electrical and Computer Engineering, University of New Mexico, Albuquerque, NM 87131.

IEEE Log Number 9144500.

High-speed UV detectors have been reported using vertical Schottky barrier [11], planar interdigitated Schottky barrier [9], Si p-n junction, and vertical p-i-n with a thin p-layer [12], with only moderate success. A promising design used a planar interdigitated Schottky barrier with a low-frequency quantum efficiency of 12% at 337 nm and a frequency response of 5.3 GHz, measured at 800 nm [9]. No picosecond impulse, autocorrelation, or heterodyne response measurements at UV wavelengths have been reported.

We report on fabrication and UV-heterodyne characterization of high-speed planar Ni-Si-Ni Schottky barrier photodetectors. For a 4.5- μm gap geometry, a 16-GHz 3-dB heterodyne response limited by packaging effects, is measured at a wavelength of 334 nm. This is the highest reported speed for an Si-based detector. A photodiode transport model, including carrier drift, diffusion, and recombination, is in good agreement with the measured detector frequency response. This model gives a 24-GHz 3-dB point for the present detector exclusive of packaging limitations. For a 1- μm gap geometry, the model predicts an 86-GHz 3-dB response for these simple Si detectors.

The detector consists of a side-by-side pair of metal-semiconductor junctions comprising a metal-semiconductor-metal (MSM) diode. The exposed semiconductor, between the metal pads, is fully depleted with an appropriate applied bias. This depleted region is the photosensitive region of the diode, and high applied fields result in very fast, saturated drift velocities of the charge carriers. It is important to appreciate that both electron and hole velocities are equally important in this configuration. In this regime, Si offers performance comparable to GaAs and InP, in contrast to the situation in which only electron velocities and mobilities are important. The direct access to the depletion region by UV photons avoids the short absorption length problem inherent in other designs.

A common phenomenon, reported for all MSM devices, is a spurious gain mechanism leading to an anomalous effective quantum efficiency, $> 100\%$, at low frequencies [9], [13]. Tentative explanations have been put forth [14], but no definitive models have been presented. This phenomenon is also seen in the devices tested in this study. Our results indicate that this gain is most likely photoconductive resulting from junction leakage; a more detailed analysis will be published elsewhere.

FABRICATION OF Ni-Si-Ni MSM SCHOTTKY BARRIER PHOTODIODES

MSM photodiodes were fabricated with Ni Schottky contacts on bulk Si ($n \sim 8 \times 10^{14} \text{ cm}^{-3}$). A planar, lateral geometry with both contacts on the top surface of the Si was

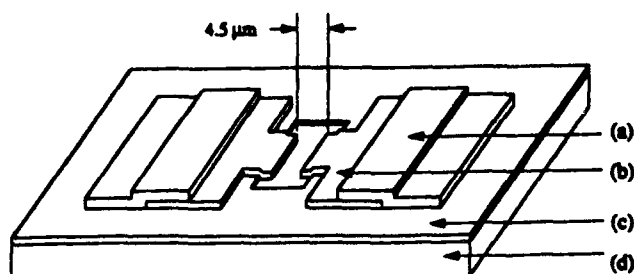


Fig. 1. MSM detector structure. Bonding pad: $75 \times 75 \mu\text{m}^2$. Window: $25 \times 20 \mu\text{m}^2$. (a) Cr/Au (200 nm). (b) Ni (30 nm). (c) SiO_2 (80 nm). (d) Si (bulk).

used; both simple-gap and interdigitated, or serpentine-gap, devices were fabricated with gap widths varying from 1 to $4.5 \mu\text{m}$. A representative structure is shown in Fig. 1. The first layer is an 80-nm-thick SiO_2 film. Windows, ranging from 100 to $500 \mu\text{m}^2$, expose the semiconductor surface where the Schottky contacts are formed. The oxide serves to isolate optically inactive metallization areas and reduce junction capacitance and dark current. The second layer is a 30-nm-thick Ni film with a series resistance of 50–60 Ω and a transmission of 17% at 334.5 nm. The Ni–Si contacts form the MSM photodiode. The photosensitive semiconductor region between the contacts varies in area from 15 to $90 \mu\text{m}^2$ in the simple-gap geometry. The final layer is a 30/170 nm Cr/Au film to form the $75 \times 75 \mu\text{m}^2$ bonding pads.

Photodiodes were fabricated using conventional photolithography, including standard liftoff techniques for metal definition. Si wafers were cleaned and inserted into a preheated furnace (1100°C), with an O_2 flow of 4 l/min, for 25 min, to grow the 80-nm oxide. The windows in the oxide film were etched, and the metal films deposited in three photolithographic steps. Metal films were deposited in an electron-beam evaporator at a rate of 0.5 nm/s.

After fabrication, wafers were cleaved to separate dies incorporating detectors with variations in geometry and dimensions. An individual die was mounted at the edge of an Au-on-alumina microstrip high-speed package using heat-conductive epoxy. The package was mounted on an Au-coated Al block and an SMA connector (18-GHz bandwidth) was pressure fitted to the strip. Gold wires (25- μm diameter) were wire bonded between the photodiode, the package, and ground. Care was taken to ensure short bond wires so that packaging inductance did not affect the measurements. Dark currents, in this nonoptimized design, were $< 50 \text{ nA}$ for a 25- μm -long device at a 10-V bias. For broad-band photodiode applications, the noise associated with this low dark current is negligible in comparison to RF-amplifier input noise.

EXPERIMENTAL ARRANGEMENT

A UV-heterodyne system was developed to characterize these detectors [15]. A single-mode Ar^+ -ion laser, $\lambda = 334.5 \text{ nm}$, and an intracavity doubled (LiIO_3), frequency stabilized dye laser provided the local oscillator and signal beams, respectively. Careful attention was placed on beam and polarization overlap. A typical local-oscillator intensity of 10^7 W/cm^2 ($\sim 2\text{-}\mu\text{m}$ FWHM) at the detector was necessary to reach shot-noise-limited detection. The gain of the RF-

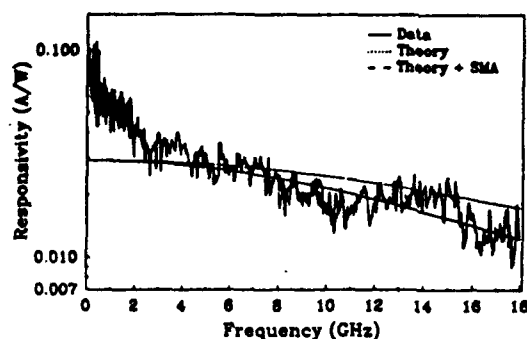


Fig. 2. Frequency response of a 4.5- μm gap interdigitated detector at 30 V bias.

amplifiers and cabling from the SMA connector to the RF-spectrum analyzer was calibrated from 1 MHz to 18 GHz using a vector network analyzer. Absolute responsivity $R(\omega)$ was confirmed by comparison to the measured dc responsivity of a well-characterized low-frequency commercial detector.

RESULTS

Measurements of $R(\omega)$ were made on several different detectors under a variety of conditions. The bulk of these measurements were used to validate an MSM detector response model that predicts high-speed detector performance as a function of bias and beam diameter and position on the detector, using Si carrier transport properties [15]. The model includes effects of carrier drift, diffusion, and recombination. A more detailed description will be published elsewhere. The model was compared to the measured frequency response for gap dimensions of 4.5, 3, and $1 \mu\text{m}$ with differing biases and beam positions.

$R(\omega)$ curves are shown for a 4.5- μm gap interdigitated detector at 30- and 10-V bias. (Figs. 2 and 3) Heterodyne signal levels were greater than 20 dB above the shot-noise floor across the entire frequency range; the $\sim \pm 1 \text{ dB}$ variations are due to package and electronics resonances as can be seen by noting the pattern similarity in the two figures. The 2- μm FWHM beam was centered in the detector gap, and $R(\omega)$ was measured out to 18 GHz. The 30-V data (Fig. 2) have been extended to show the low-frequency gain region, inherent in all MSM photodiodes. Two theoretical plots are shown. The upper curve in both graphs is the detector model which is in good agreement with the data out to about 14 GHz. At these frequencies, the bandwidth limitations of the SMA connector on the detector package become important. The SMA connector-detector package can be modeled as the product of a simple single pole, with a characteristic frequency of 18 GHz, due to the SMA connector, and the detector response. This leads to the lower modeling curve. An excellent fit is obtained out to the experimental frequency limit of 18 GHz, constrained by available amplifiers. The effect of the SMA connector can be seen on both the 30- and 10-V data. The variation in the frequency response for these two cases arises because of the (slight) change in carrier velocities at the two applied field strengths in this saturated regime. The only adjustable parameter is the overall quantum efficiency.

An extrapolation of the detector bandwidth can be made

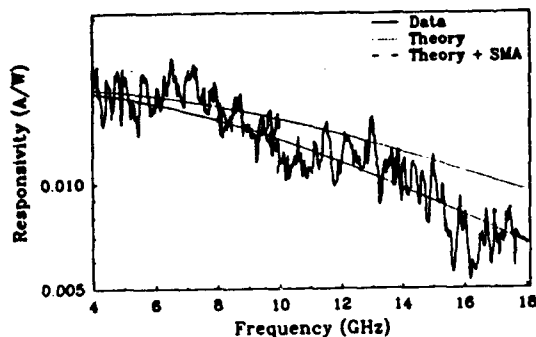


Fig. 3. Frequency response of a 4.5- μm gap interdigitated detector at 10 V bias.

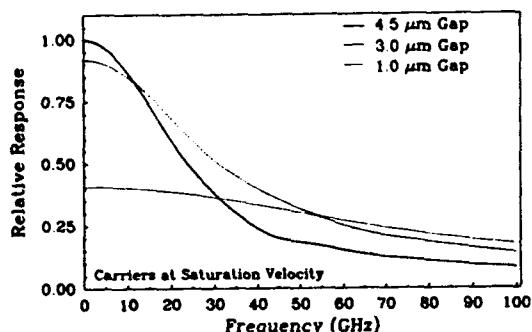


Fig. 4. Theoretical frequency response curves for varying gap dimensions. The calculation was carried out for a fixed 2- μm illumination spot and a fixed bias of 10^4 V/cm. The reduced responsivity for the smaller detectors is simply a geometrical effect due to the reduced overlap between the beam and the active detector area.

from the model, assuming an ideal RF package. At 30-V bias, the bandwidth of this 4.5- μm gap detector is 21.5 GHz. Increasing the bias will result in slightly higher carrier velocities and should give a 24-GHz bandwidth for a 4.5- μm gap Si-based detector. Scaling the response to smaller detector gap widths of 3 and 1 μm , the model predicts bandwidths of 34 and 86 GHz, respectively (cf. Fig. 4). The lower responsivity shown for the smaller detectors is simply a geometrical effect as the calculation is carried out for a fixed incident spot size. This high-speed response is comparable to the fastest reported GaAs detectors. The high-frequency ultraviolet responsivity of these detectors, 0.032 A/W ($\sim 12\%$ quantum efficiency) with no antireflective coating, is very high for detectors with these large bandwidths. The quantum efficiency of the smaller gap detectors scales only with the gap dimension/spot size ratio. Thus, if the incident spot is smaller than the gap dimension, then the quantum efficiency remains nearly constant. Smaller detectors and tighter focusing will lead to a significantly improved quantum-efficiency bandwidth product.

CONCLUSION

A high-speed MSM photodiode, based on bulk Si and fabricated by a simple, inexpensive process, has been demonstrated. The bandwidths of these devices compare well to the fastest reported GaAs devices. A major advantage of this device for UV applications is the relative robustness of Si compared to GaAs when subjected to intense ultraviolet radiation. GaAs devices were also fabricated; however, they showed severe degradation, on a time scale of minutes, when subject to the intense local oscillator irradiation. This degra-

dation was irreversible and severely limits the applicability of the unpassivated GaAs devices for ultraviolet applications. In contrast, the Ni-Si devices were extremely robust with no changes in speed or responsivity observed over time scales of several months—both for devices stored in laboratory ambient and devices subjected to many hours of high-intensity UV irradiation.

The simplicity, manufacturability, interconnection compatibility, and robustness of the planar-Si MSM photodiode make it a strong candidate for applications where the ultimate connection is to a silicon VLSI circuit. The high-speed high-responsivity detector presented here is an ideal candidate for many applications due to its materials compatibility with standard Si technology and the absence of complex and expensive epitaxial growths.

ACKNOWLEDGMENT

Helpful discussions with D. L. Spears and V. Diadiuk are gratefully acknowledged. C. F. Schaus provided extensive guidance in device design.

REFERENCES

- [1] W. Lenth, A. Chu, L. J. Mahoney, R. W. McClelland, R. W. Mountain, and D. J. Silversmith, "Planar GaAs p-i-n photodiode with picosecond time response," *Appl. Phys. Lett.*, vol. 46, pp. 191-193, 1985.
- [2] R. S. Tucker, A. J. Taylor, C. A. Burrus, G. Eisenstein, and J. M. Wiesenfeld, "Coaxially mounted 67 GHz bandwidth InGaAs PIN photodiode," *Electron. Lett.*, vol. 22, pp. 917-918, 1986.
- [3] S. Y. Wang and D. M. Bloom, "100-GHz bandwidth planar GaAs Schottky photodiode," *Electron. Lett.*, vol. 19, pp. 554-555, 1983.
- [4] D. G. Parker, P. G. Say, A. M. Hansom, and W. Sibbett, "110 GHz high-efficiency photodiodes fabricated from indium tin oxide/GaAs," *Electron. Lett.*, vol. 23, pp. 527-528, 1987.
- [5] T. Sugeta, T. Urisu, S. Sakata, and Y. Mizushima, "Metal-semiconductor-metal photodetector for high-speed optoelectronic circuits," *Japan. J. Appl. Phys.*, vol. 19, suppl. 19-1, 1980.
- [6] B. J. Van Zegbroeck, C. Harder, J.-M. Halbout, H. Jakel, H. Meier, W. Patrick, P. Vettiger, and P. Wolf, "5.2 GHz monolithic GaAs optoelectronic receiver," in *Tech. Dig., IEEE IEDM*, 1987, pp. 229-232.
- [7] O. Wada, H. Hamaguchi, L. LaBella, and C. Y. Boisrort, "Noise characteristics of GaAs metal-semiconductor-metal photodiodes," *Electron. Lett.*, vol. 24, p. 1574, 1988.
- [8] J. C. Campbell, W. S. Holden, G. J. Qua, and A. G. Dentai, "Frequency response of InP/InGaAsP/InGaAs avalanche photodiodes with separate absorption, grading and multiplication regions," *IEEE J. Quantum Electron.*, vol. QE-21, pp. 1743-1746, 1985.
- [9] R. J. Seymour and B. K. Gariside, "Ultrafast silicon interdigital photodiodes for ultraviolet applications," *Can. J. Phys.*, vol. 63, pp. 707-711, 1985.
- [10] G. E. Bulman, D. R. Myers, T. E. Zipperian, and L. R. Dawson, "Proton isolated $\text{In}_{0.2}\text{Ga}_{0.8}\text{As}$ /GaAs strained-layer superlattice avalanche photodiode," *Appl. Phys. Lett.*, vol. 48, pp. 1015-1017, 1986.
- [11] H. Fabricius, T. Skettrup, and P. Bagaard, "Ultraviolet detectors in thin sputtered ZnO films," *Appl. Opt.*, vol. 25, pp. 2764-2767, 1986.
- [12] C.-Y. Wingo, C. Salupo, L. F. Szabo, G. P. Caesar, and W. Javurek, "A new type of stable and sensitive UV detector fabricated with amorphous silicon-based alloys," presented at the MRS Spring Meet., 1988.
- [13] D. K. Donah, S. Y. Wang, T. R. Ranganath, S. A. Newton, and W. R. Tuttle, "Photocurrent amplification in Schottky photodiodes," *Appl. Phys. Lett.*, vol. 49, pp. 567-568, 1986.
- [14] M. Ito and O. Wada, "Low dark current GaAs metal-semiconductor-metal (MSM) photodiodes using WSi_2 contacts," *IEEE J. Quantum Electron.*, vol. QE-22, pp. 1073-1077, 1986.
- [15] B. W. Mullins, "Heterodyne characterization of high speed photomixers for the ultraviolet," Ph.D. dissertation, Dep. Phys., Univ. New Mexico, 1989 (unpublished).

Grating coupling to surface plasma waves.

I. First-order coupling

Saleem H. Zaidi

Center for High Technology Materials, University of New Mexico, Albuquerque, New Mexico 87131

M. Yousaf*

Department of Physics, University of New Mexico, Albuquerque, New Mexico 87131

S. R. J. Brueck

Center for High Technology Materials, University of New Mexico, Albuquerque, New Mexico 87131

Received May 17, 1990; accepted October 18, 1990

A systematic experimental and theoretical study of first-order grating coupling to surface plasma waves existing at an air-Ag interface is presented. The experiment extends beyond previous work to grating depths comparable with the grating period. The grating profiles range from sinusoidal to rectangular. For TM-polarized incident radiation this grating depth range includes the entire spectrum of surface-plasma-wave-radiation coupling—from underdamped, to nearly 100% coupling, to overdamped and the disappearance of the resonance from the zero-order reflectance measurements. Strong polarization and absorption effects are observed for the deepest gratings. A simple theoretical model, based on the Rayleigh hypothesis and retaining only resonant diffraction terms without a small-signal approximation being made, provides good agreement with the experimental results.

INTRODUCTION

The study of the interaction of light with periodic structures (gratings) on metals has a long and distinguished history. In 1902 Wood¹ first noted the anomalous behavior (christened Wood's anomalies) displayed by diffraction gratings of large and rapid changes in diffraction intensities for small angular and spectral variations. Rayleigh^{2,3} presented in 1907 the first theoretical explanation of these anomalies in suggesting that such behavior was due to the cutoff or the appearance of a new spectral order. In 1941 Fano first distinguished between two types of Wood anomalies: (1) an edge anomaly, with a sharp behavior related to the passing off of a diffraction order (i.e., a diffraction order passing over the horizon, 90° to the surface normal) and (2) a resonance anomaly due to excitation of a bound or surface wave at the metal-dielectric interface.⁴

Surface plasma waves (SPW's) are TM modes of the electromagnetic field bound to the interface between a metal and a dielectric. The condition for existence of the SPW mode is $\epsilon_m' < -\epsilon_d$, where ϵ_m' is the real part of the metal dielectric constant and ϵ_d is the dielectric constant of the dielectric. Related modes, first investigated by Sommerfeld,⁵ exist when one of the media is highly lossy. The SPW phase velocity is less than the light velocity in the dielectric, and phase matching between an incident, freely propagating wave and the SPW is accomplished either by a prism⁶ or by grating coupling techniques.

The SPW dispersion relation for a planar metal-air interface is simply given by⁷

$$k_{\text{SPW}} = k_0[\epsilon_m/(\epsilon_m + 1)]^{1/2}, \quad (1)$$

where $k_0 = 2\pi/\lambda$ is the free-space optical wave vector. The phase-matching condition for excitation of SPW's is satisfied whenever $k_0 \sin \theta$, the component of k_0 along the metal-air interface, satisfies the condition

$$k_0 \sin \theta = \pm k_{\text{SPW}}' + n2\pi/d, \quad (2)$$

where d is the grating period, θ is the angle of incidence, $n = \pm 1, \pm 2, \dots$ is the coupling order, and k_{SPW}' is the real part of the SPW wave vector. In Eq. (2) the choice of a negative sign preceding k_{SPW}' corresponds to a SPW moving in the direction opposite the incident wave. This expression assumes that the grating wave vector is in the plane of incidence; i.e., the grating lines are perpendicular to the incident wave vector.

The SPW dispersion relationship is plotted in Fig. 1 for a lossless, free-electron metal ($\epsilon_m = 1 - \omega_p^2/\omega^2$), where the axes are normalized to the plasma frequency ω_p and the corresponding optical wave vector ($k_p = \omega_p/c$). Also shown as two vertical dashed lines, corresponding to the $n = \pm 1$ orders in Eq. (2), are the wave vectors of a surface grating. Finally, the wave vectors accessible in the $n = 0$ and $n = \pm 1$ orders by variations in the angle of incidence are shown as horizontal lines. This figure was drawn for a grating period smaller than the optical wavelength ($\lambda/d > 1$); note that there is only one point that satisfies Eq. (2), for $n = -1$, and at this incident angle there is no allowed diffraction order.

In 1967 Teng and Stern first detected SPW's optically by bombarding 1200-line/mm (833-nm-period) gratings with 10-keV electrons and observing the emitted optical radiation.⁸ They observed that the line shape of the

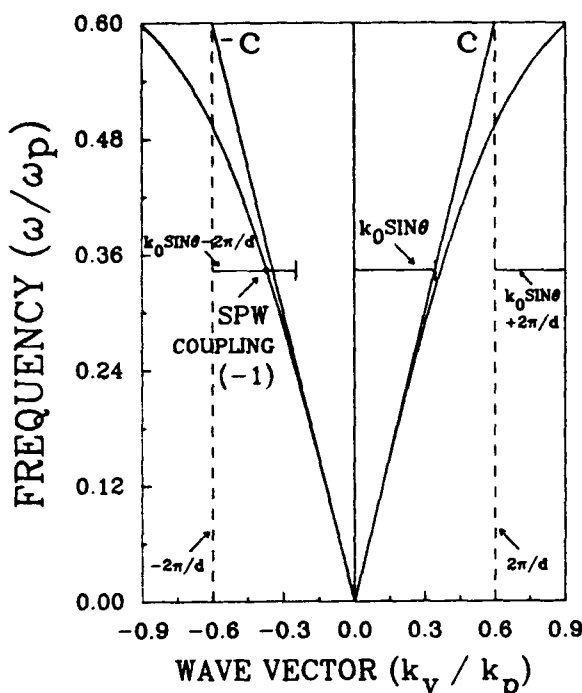


Fig. 1. Dispersion relation of SPW's for a lossless, free-electron metal ($\epsilon = 1 - \omega_p^2/\omega^2$). The axes are normalized to ω_p and $k_p = \omega_p/c$. The grating wave vectors corresponding to $n = \pm 1$ order of a grating of period d are shown as vertical dashed lines. The range of wave vectors accessible by variations in the input angle from normal to grazing incidence for $n = 0$ and $n = \pm 1$ is shown as horizontal lines. Note that for this choice of parameters ($\lambda/d < 1$) there is only one SPW coupling resonance, and at this resonance angle there is no propagating diffraction order.

emitted radiation was influenced by the surface condition of the metal but was independent of the energy of the bombarding electrons. Cowan and Arakawa carried out a detailed study of the SPW dispersion curves for dielectric-metal layers on concave diffraction gratings and also developed a quantum-mechanical formalism to describe their results.⁹ Hutley and co-workers published in 1973 a detailed experimental study of the anomalies of sinusoidal profile gratings as a function of grating depth¹⁰⁻¹² and characterized the SPW line shapes for grating depths h ranging up to 60 nm for 500-nm-period gratings ($h/d \leq 0.12$). The integral formalism developed by Petit and others¹³ was used to describe these results with good agreement. Pockrand and Raether, in an extensive series of publications,¹⁴⁻¹⁸ characterized the SPW coupling as a function of grating period, depth, and profile. The gratings studied were sufficiently deep for better than 98% coupling into the SPW mode to be realized. A perturbation analysis, developed by Kroger and Kretschmann,¹⁹ was used in modeling these results with good agreement, although clearly the perturbation approach must break down as the coupling efficiency approaches 100%. A complete theoretical treatment of grating coupling to SPW's was provided by Mills and co-workers.^{20,21} Their approach uses an integral formulation of the boundary-value problem at the grating interface and an extinction theorem mechanism following from Green's theorem that was first applied by Toigo *et al.*²² The latter study does not give simple analytic results but relies on extensive computational and numerical evaluation. Glass *et al.*²³ and

Weber²⁴ simplified this treatment by developing a renormalized mode-coupling theory that retained the resonant terms and treated all other terms within perturbation theory. Yamashita and Tsuji²⁵ independently developed a differential formulation that treats the resonantly generated fields on a par with the incident fields and allows for saturation and decreases in coupling with increasing grating depths. They employed a power-series expansion in $k_0 h$ and restricted their study to small grating amplitudes; simple analytic expressions were obtained for the coupling strength as a function of h .

In this paper a comprehensive experimental and theoretical study of first-order grating coupling to SPW's for a wide range of grating parameters is presented. The experimental results establish, for the first time to our knowledge, a relationship between grating depth and grating period for SPW coupling and extend to grating depths that no longer support SPW's but rather show polarization and absorption effects. The theoretical approach is an extension of the Rayleigh hypothesis including only resonant terms in the Rayleigh expansion (cf. Refs. 23-25). This results in considerable simplification; reasonable agreement between theory and experiment is found out to depth/period ratios of ~ 0.5 . Gupta *et al.*²⁶ used a similar approach to describe grating coupling to long-range SPW modes on thin, symmetrically bounded, metal films.

GRATING FABRICATION

Gratings were fabricated holographically in positive photoresist layers spun onto Si substrates with the use of the 488-nm line from a single-mode Ar-ion laser. The details of the grating fabrication were presented elsewhere.²⁷ The grating profiles were approximately sinusoidal for shallow depths, evolving toward rectangular profiles as the depth was increased (cf. Fig. 4 below). After development these gratings were coated with ~ 100 -nm-thick electron-beam evaporated Ag films. Films were deposited at room temperature and at background pressures of low 10^{-6} Torr.

OPTICAL ARRANGEMENT

All of the measurements reported here are of the angular dependence of the zero-order reflectance for a fixed-frequency TM-polarized He-Ne laser beam at 633 nm. The samples were mounted as one surface in a 90° corner reflector attached to a computer-controlled rotation stage. This arrangement ensured that the reflected beam was always returned in the same direction and eliminated the necessity of a second rotation stage for the detector. The incident laser beam was focused with a long-focal-length (0.5-m) lens to a spot of ~ 2 mm. This provided an angular limitation of 0.05° , much smaller than the observed reflectance variations. Care was taken with the alignment to ensure that the axis of the rotation stage was in the plane of the grating so that the laser spot sampled the same area of the grating throughout a scan. Grating depths were measured in cross section with a scanning electron microscope (SEM). This introduces some errors, estimated at ± 5 nm, owing to uncertainties in the SEM calibration and variations in the grating depth for the different areas sampled in the optical and SEM measurements.

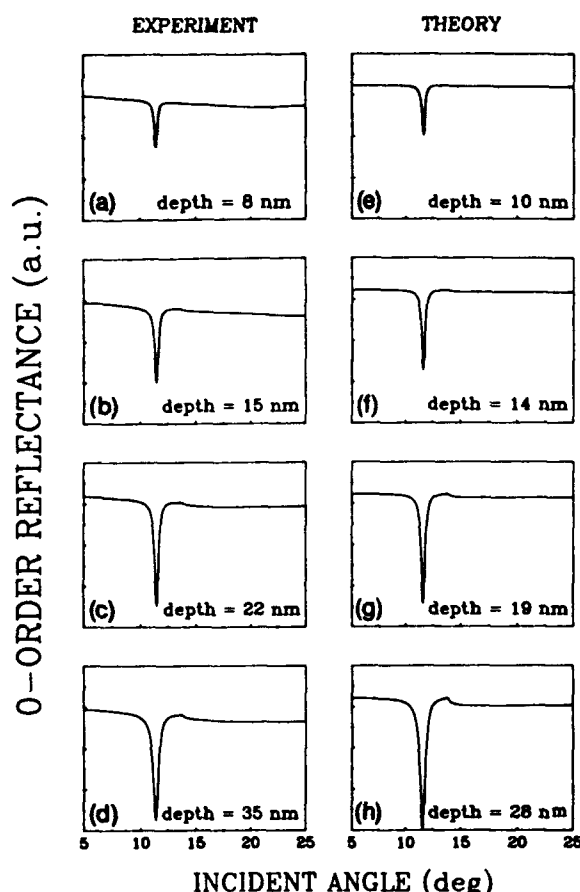


Fig. 2. Zero-order reflectance at 633 nm for 510-nm-period gratings with varying grating depths. The left side [(a)–(d)] presents experimental results; the right side [(e)–(h)] presents theoretical modeling. See the text for details.

EXPERIMENTAL RESULTS

Zero-order reflectance measurements for a series of 510-nm gratings with increasing depth are shown on the left-hand side of Fig. 2. The theoretical modeling shown on the right-hand side will be discussed below. The major features to be noted in these measurements include the following:

- (1) The excitation of SPW's at $\theta \sim 11.6^\circ$ corresponding to the sharp dip in the reflectivity (note that there is no diffracted order at this angle, so that this decrease corresponds directly to energy coupled into the SPW mode),
- (2) The rapid increase in coupling efficiency with increasing grating depth to a maximum observed coupling of 94% at a grating depth of 35 nm,
- (3) The horizon for the $n = -1$ diffracted order at $\theta \sim 13.8^\circ$ (this is apparent as the cusp in the reflectivity as energy is transferred from the specularly reflected beam to the diffracted beam).

Similar results for deeper gratings are presented on the left-hand side of Fig. 3. Note the larger angular scale in this figure. Specific features to be noted include the following:

- (1) The relatively gradual decrease in the coupling efficiency of SPW's,
- (2) The clear broadening of the SPW resonance with increasing depth,

(3) The shift in the SPW resonance to smaller angles with increasing depth,

(4) The residual SPW coupling even at large grating depth/grating period ratios,

(5) The increasing coupling to the $n = -1$ diffraction order. (The sharp spike at $\sim 38^\circ$ corresponds to the collection of the $n = -1$ diffraction order in the optical system and is not part of the zero-order reflectance. It does provide a useful monitor of the energy in the diffracted order.)

SEM images of the gratings used for the measurements of Fig. 3, taken in cross section, are shown in Fig. 4. Note that the grating shapes are sinusoidal at low depths but gradually show increasing harmonic components and trend toward rectangular profiles for the deepest gratings investigated. This profile modification results from the grating fabrication technique.²⁷

Similar experiments were performed for gratings with periods of 392 and 440 nm, in an investigation of the dependence of the coupling efficiency on grating depth and grating period. All the experiments were carried out at a wavelength of 633 nm, in avoidance of variations in the metal optical properties. Qualitatively similar behavior was observed, with comparable coupling efficiencies occurring at shallower grating depths for finer gratings. Experimentally determined coupling efficiencies, resonance angles, and resonance linewidths for all three sets

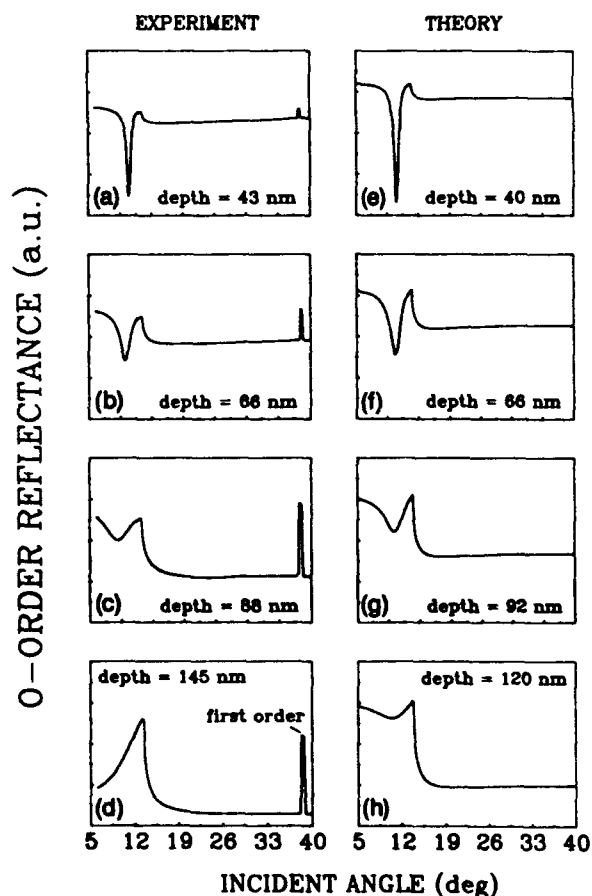


Fig. 3. Continuation of Fig. 2 for deeper gratings. Note the expanded angular scale. Again, the left side [(a)–(d)] presents experimental results; the right side [(e)–(h)], theoretical modeling. The sharp spikes on the experimental data at $\sim 38^\circ$ correspond to the $n = -1$ diffraction order entering the collection optics and are not a part of the zero-order reflectivity.

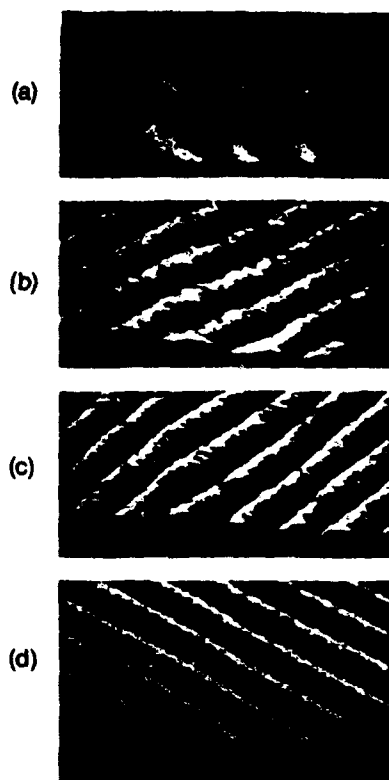


Fig. 4. Cross-section SEM pictures of the gratings used for the experiments. The measured depths are (a) 43 nm, (b) 57 nm, (c) 88 nm, and (d) 145 nm.

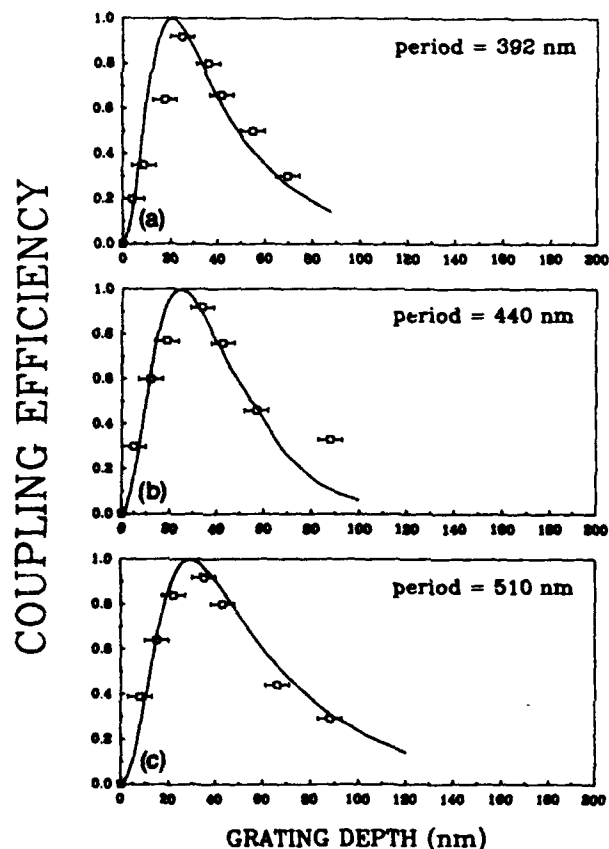


Fig. 5. Coupling efficiency into the SPW mode for gratings with periods of (a) 392 nm, (b) 440 nm, and (c) 510 nm and varying depths. The solid curves are the result of theoretical modeling; see the text for details.

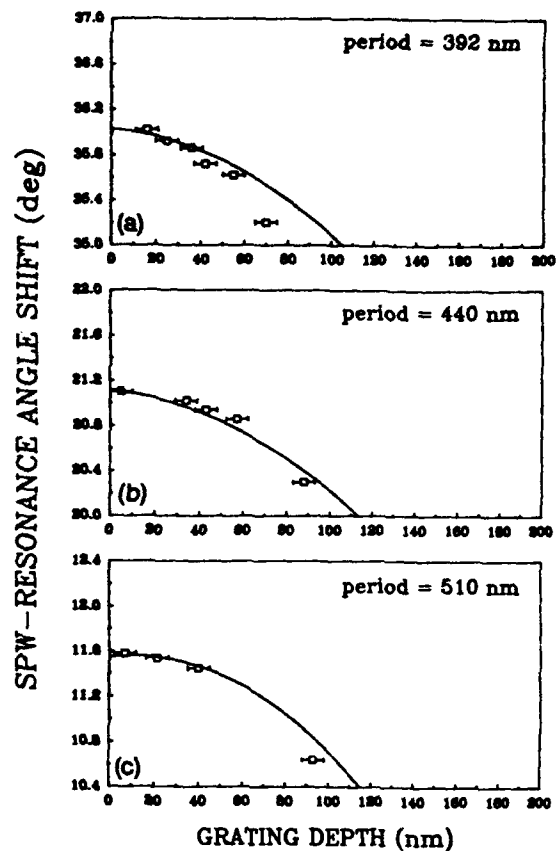


Fig. 6. Same as Fig. 5, except here for SPW resonance angle.

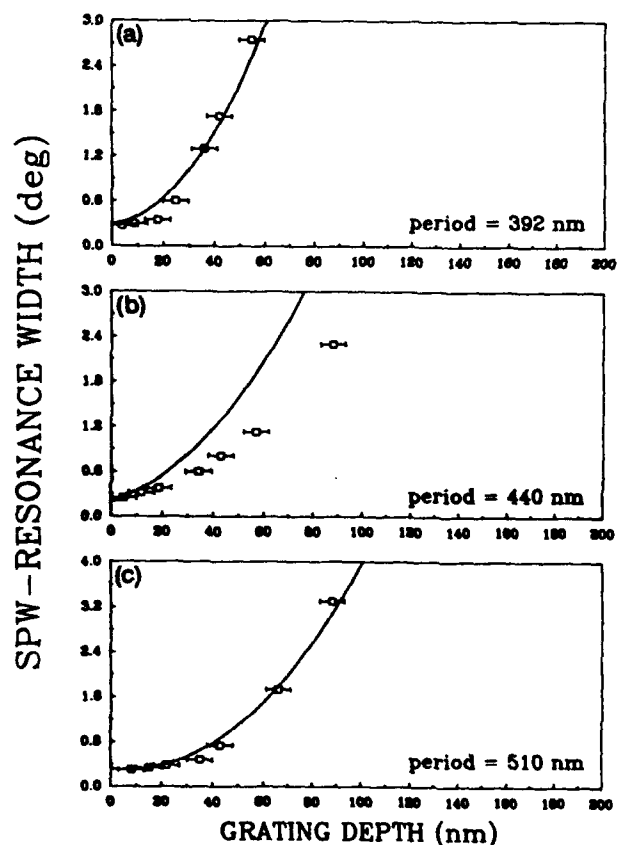


Fig. 7. Same as Fig. 5, except here for SPW resonance linewidth (FWHM).

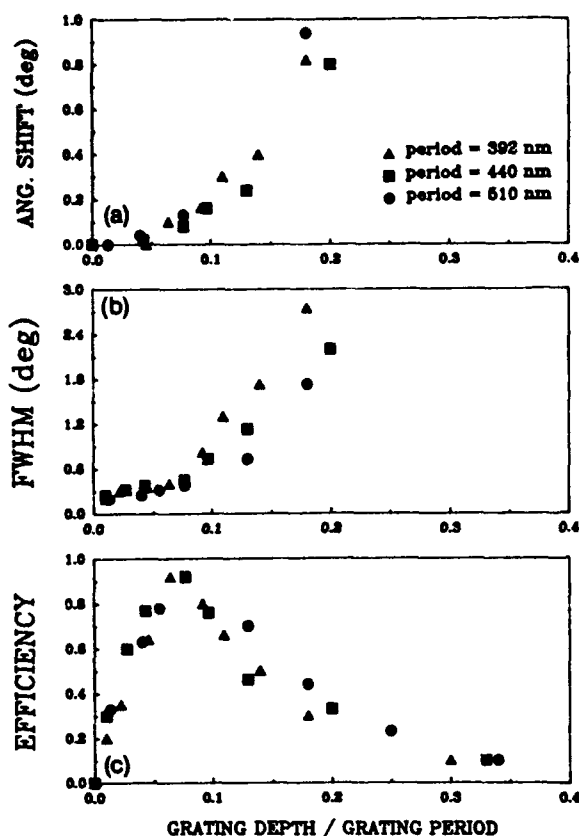


Fig. 8. Data of Figs. 5–7 for the SPW resonance angle, the resonance linewidth, and the coupling efficiency replotted against the dimensionless parameter h/d . Note that this parameter is approximately invariant for these three grating periods.

of gratings are presented in Figs. 5, 6, and 7, respectively. The solid curves are theoretical and will be discussed below. With increasing grating depth each of the data sets displays an initial rapid increase in coupling efficiency, peaking at over 90%, and a slower decrease in efficiency; an approximately quadratic decrease in the resonant coupling angle; and an approximately quadratic increase in the resonance width.

These results are summarized in Fig. 8, which shows all three sets of data plotted against the dimensionless parameter h/d , i.e., grating depth/grating period. Within experimental uncertainties these results appear to follow a common behavior. Some of the variability may well arise from differing grating profiles, especially for the deeper gratings.

Further increases in grating depth, accompanied by a change in profile to rectangular, lead to an elimination of SPW effects. For approximately square gratings strong polarization effects demonstrate the possibility of the fabrication of reflective polarizers for visible radiation. This is shown in Fig. 9, where reflectance scans for the three grating periods are given for depths of 200 nm (392-nm period), 170 nm (440-nm period), and 190 nm (510-nm period), which resulted in maximum polarization effects. Note that for TM polarization, almost 100% of the incident energy ($\sim 98\%$ for the 510-nm-period grating) is coupled into the first-order diffraction peak for angles beyond the horizon for this order. In contrast, only approximately 20% of the energy polarized in the TE direction is coupled out of the zero-order reflected beam. Careful

variations of grating depth and profile must be investigated for optimization of the polarization of the reflected beam. Such polarization behavior for square gratings was predicted^{24,29} and demonstrated in the infrared³⁰; to our knowledge, though, this is the first observation of these effects in the visible spectral region. SEM pictures of the gratings are shown in Fig. 10.

Further increases in grating depth result in rectangular profiles with decreasing line/space ratios. Angular reflectance scans for deep rectangular gratings are shown in Fig. 11 [(a) 320-nm depth, 392-nm period; (b) 330-nm depth, 440-nm period; (c) 300-nm depth, 510-nm period]. There is a broad absorption of TM-polarized radiation, while a large diffraction efficiency, increasing with increasing periods, is observed for TE polarization. Figure 12 shows SEM pictures of these gratings.

THEORY

During the past thirty years many grating theories based on the vector character of the electromagnetic field have been developed. An excellent summary can be found in Refs. 6, 13, and 20. Integral methods, developed by Petit and others, evaluate the field at any point in terms of an integral over the grating surface Λ (cf. Fig. 13). A variation of these integral techniques based on a Green's-function formalism specifically directed to the evaluation of the SPW dispersion relation on a periodic surface was extensively developed by Mills and co-workers^{20,21} and Otagawa.³¹ In addition, a differential formalism, developed by Nevierre *et al.*,³² was applied to SPW's on a periodic surface by Numata.³³ All these approaches are fully rigorous, hold for arbitrary profiles, and require exten-

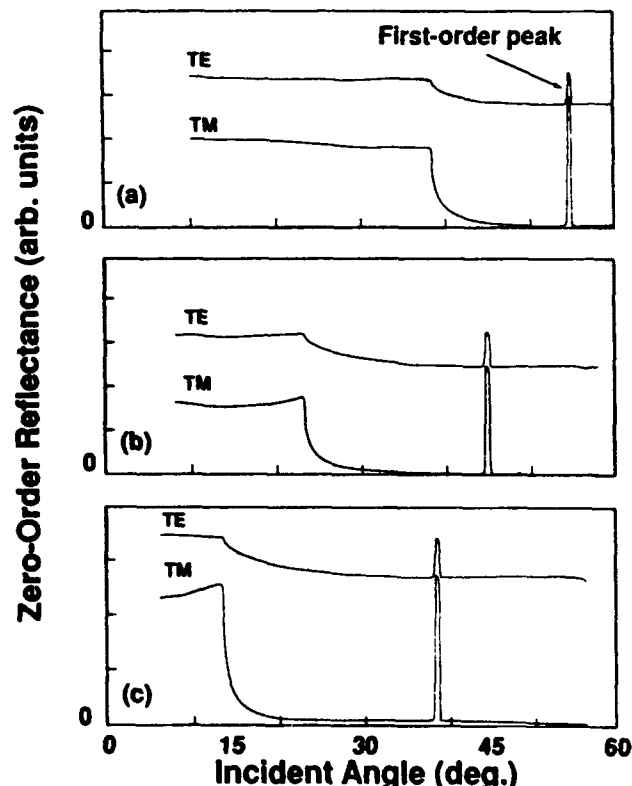


Fig. 9. Sequence of zero-order reflectance scans for approximately square gratings ($h/d \sim 0.5$) showing strong polarizing effects: (a) $h = 200$ nm, $d = 392$ nm; (b) $h = 170$ nm, $d = 440$ nm; and (c) $h = 190$ nm, $d = 510$ nm.

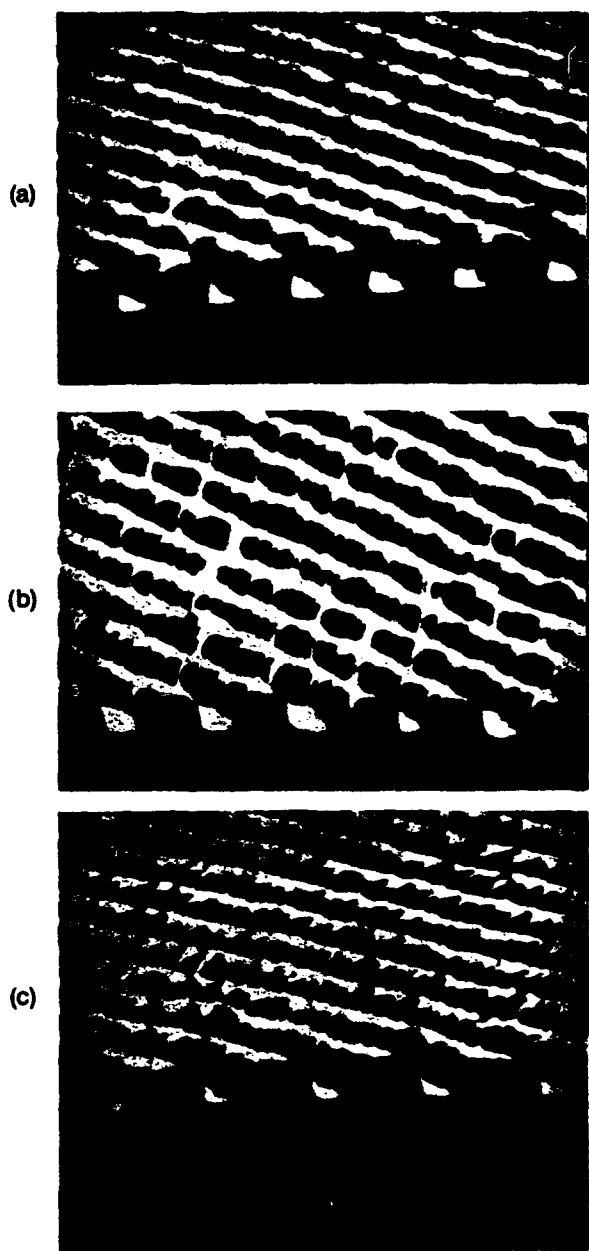


Fig. 10. SEM pictures of the gratings used for the measurements of Fig. 9

sive computation, typically involving matrices of order 40 or higher.

A number of differential analyses, usually based on a perturbation expansion in $k_0 h$, where h is the grating depth, and relying on a Rayleigh or plane-wave approach have also been presented.^{19,24,25} In these treatments the scattered field amplitudes are also treated as small quantities, of the order of $k_0 h$ times the incident and reflected/transmitted field amplitudes. These models have the virtue of relatively simple analytic results and ready physical interpretation. These perturbational approaches clearly break down as the coupling efficiencies into SPW modes and diffraction orders approach unity, since they do not self-consistently describe the necessary decrease in the zero-order reflected and transmitted beams. Yamashita and Tsuji²⁶ treated the coupling problem within the Rayleigh hypothesis without making the small-signal approximation for the resonant scattered fields;

however, their treatment retained the expansion in $k_0 h$, which limits its applicability to larger grating amplitudes. Nevertheless, their model provided an elegant analytic result that included the quadratic $[\alpha(k_0 h)^2]$ increase in the SPW intensity with grating depth for shallow gratings, the saturation of the SPW intensity at a coupling efficiency near 100%, and a gradual decrease of the coupling $[\alpha(k_0 h)^{-2}]$ for deeper gratings as the energy is coupled back into the radiating fields, in qualitative agreement with the experimental results presented above. Weber²⁴ presented a related analysis, based on the extinction theorem, that retains the nonresonant terms in a perturbation-theory expansion in $k_0 h$ while also keeping the resonant terms.

These models begin with a time-harmonic, plane-wave expansion of the electromagnetic field in the regions outside the grating kerf ($z < 0$ and $z > h$, Fig. 13); the magnetic fields of the TM-polarized fields are given by

$$B^v = B^v e_z = \{ \exp[i(k_y y + k_z z)] + \sum B_n^v \exp[i(k_n y - \alpha_n z)] \} e_z, \quad z < 0 \quad (3a)$$

and

$$B^w = B^w e_z = \sum B_n^w \exp[i(k_n y + \beta_n z)] e_z, \quad z > h, \quad (3b)$$

where $k_y = k_0 \sin \theta$, $k_z = k_0 \cos \theta$, $k_n = k_y + ng$, $n = 0, \pm 1, \pm 2, \dots$, $g = 2\pi/d$ is the grating wave vector with d the grating period, $\alpha_n = (k_n^2 - k_0^2)^{1/2}$, $\beta_n =$

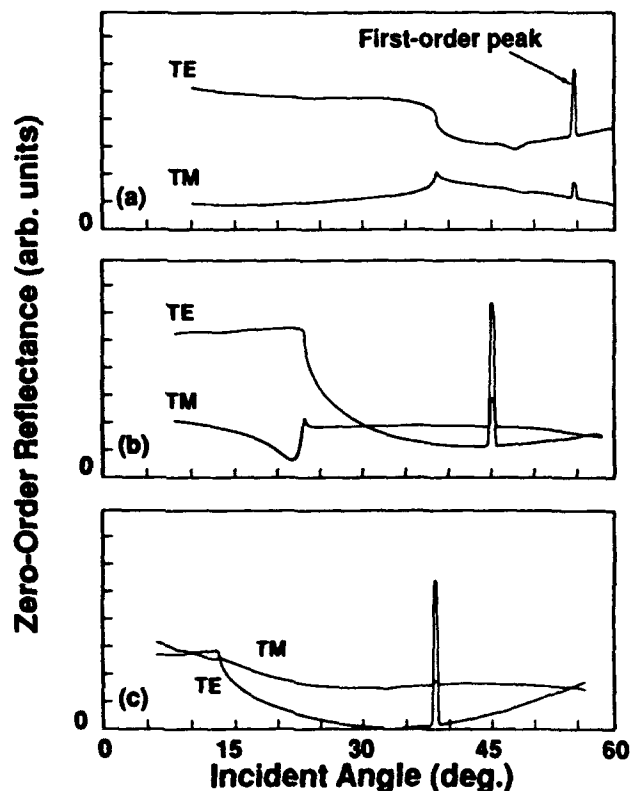


Fig. 11. Sequence of zero-order reflectance scans for deeper rectangular gratings ($h/d \sim 1$) showing strong absorption effects: (a) $h = 320$ nm, $d = 392$ nm; (b) $h = 330$ nm, $d = 440$ nm; and (c) $h = 300$ nm, $d = 510$ nm.

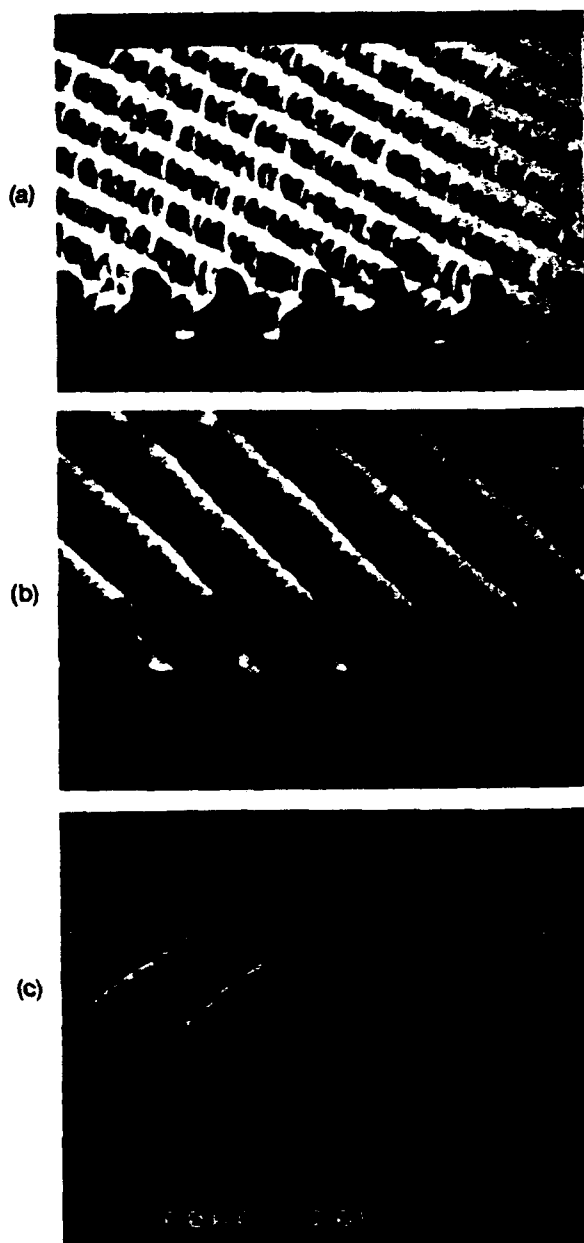


Fig. 12. SEM pictures of the gratings used for the measurements of Fig. 11.

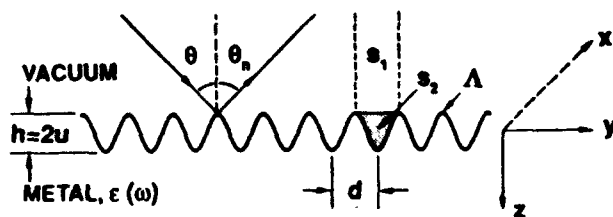


Fig. 13. Geometry used in the analysis.

$\epsilon(k_n^2 - \epsilon_m k_0^2)^{1/2}$, and ϵ_m is the metal dielectric constant. Within the grating kerf ($0 < z < h$), the validity of this expansion is not well established. Rayleigh made the assumption, known as the Rayleigh hypothesis, that for sufficiently shallow gratings this expansion is valid everywhere. This hypothesis was investigated by Van den Berg and Fokkema³⁶ and shown to be analytically correct; Petit

and Cadilhac³⁶ showed that for TE polarization the Rayleigh expansion is convergent for $h/d < 0.14$, and pointed out that reliable results could be obtained even for h/d values as great as twice this limit. A detailed analysis of the applicability of the Rayleigh hypothesis to real materials was recently presented.³⁷ Glass et al.³⁸ pointed out that the extinction theorem formalism leads to the identical dispersion relation.

The approach used here in the comparison with experiment is to apply the Rayleigh hypothesis for TM-polarized input radiation. For the gratings used in these experiments, h/d extends to 0.8, although detailed comparisons are attempted only to ~ 0.3 . The calculation does not make a small-signal approximation for either the grating depth or the diffracted field amplitudes. The plane-wave expansion [Eqs. (3)] is truncated by the retention of resonant terms, e.g., $n = 0$ and $n = -1$. In addition, the next terms, $n = -2$ and $n = +1$ are retained in the numerical evaluations and are determined to be small relative to the resonant terms. Energy conservation, i.e., a constant total of the energies in the diffracted beams and absorbed in the metal, is used as a further check on the calculation.

Thus Eq. (3) is assumed to hold up to the grating surface defined by

$$f(y) = u \sin(gy), \quad (4)$$

where $u = h/2$ is the grating amplitude. Using the generating function for Bessel functions, we can write

$$\exp[i\gamma f(y)] = \exp[i\gamma u \sin(gy)] = \sum \exp(ipgy) J_p(\gamma u). \quad (5)$$

The boundary conditions satisfied by these fields are

$$\{B^v(y, z) = B^m(y, z)\}|_{z=f(y)} \quad (6)$$

and

$$\left\{ \frac{\partial B^v(y, z)}{\partial n} = \frac{1}{\epsilon_m} \frac{\partial B^m(y, z)}{\partial n} \right\} \Big|_{z=f(y)}, \quad (7)$$

where

$$\frac{\partial}{\partial n} = \left[1 + \left(\frac{\partial f}{\partial y} \right)^2 \right]^{-1/2} \left(\frac{\partial}{\partial z} - \frac{\partial f}{\partial y} \frac{\partial}{\partial y} \right).$$

Applying these boundary conditions leads to an infinite set of coupled linear equations:

$$J_p(k, u) + \sum B_n^v (-1)^{p-n} J_{p-n}(\alpha_n u) - \sum B_n^m J_{p-n}(\beta_n u) = 0 \quad (8)$$

and

$$\left(k_z - \frac{pgk_z}{k_s} \right) J_p(k, u) - \sum \left[\alpha_n - \frac{(p-n)gk_z}{\alpha_n} \right] B_n^v (-1)^{p-n} J_{p-n}(\alpha_n u) - \frac{1}{\epsilon_m} \sum \left[\beta_n - \frac{(p-n)gk_z}{\beta_n} \right] B_n^m J_{p-n}(\beta_n u) = 0, \quad (9)$$

where p and n are integers extending from $-\infty$ to $+\infty$.

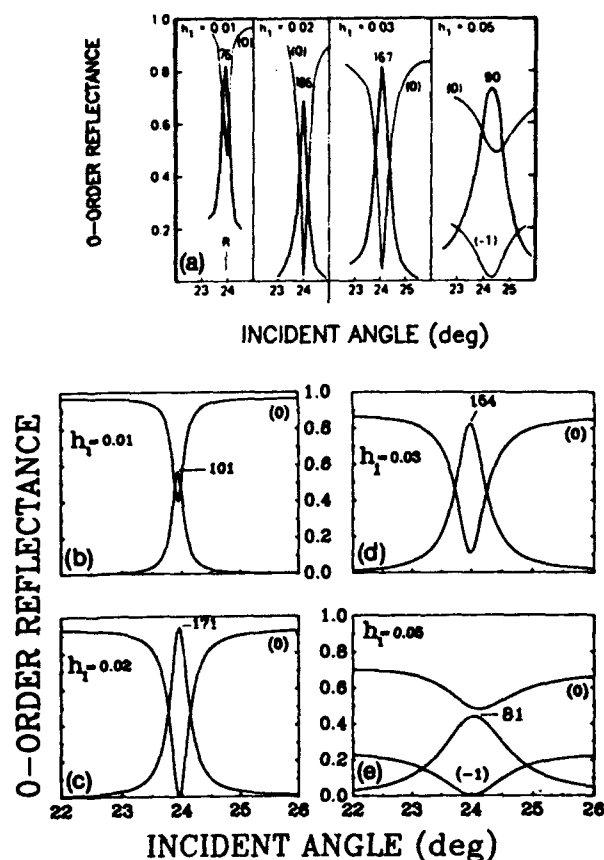


Fig. 14. Comparison of (a) calculations of Garcia³⁸ with [(b)-(e)] present calculations for 800-nm-period Au gratings at 633 nm ($h_1 = h/2d$).

Note that no small-signal approximation was made in the derivation of these equations. These equations are now truncated by the retention of only the fields for $n = 0$ and $n = -1$, the reflected/transmitted and resonant diffracted terms, which are expected to be large based on phase-matching arguments [cf. Eq. (2) and Fig. 1]. In addition, the fields for $n = +1$ and $n = -2$ were retained as a check on the convergence. The relative field intensities for these two orders for a 510-nm-period grating at a depth of 22 nm were 0.017 and 0.0018, respectively, lending support to this truncation procedure. This leads to solving an 8×8 matrix inversion for the field intensities.

Using the Green's-function approach developed by Toigo et al.,²² Garcia evaluated the SPW fields and line shape for sinusoidal gratings.³⁸ The results, obtained by the inclusion of 60 terms in the numerical analysis, are shown in Fig. 14(a) for parameters appropriate to an 800-nm-period Au grating of various depths $h_1 = h/2d$. For this grating period and wavelength (633 nm), $\lambda/d < 1$, and there are two possible propagating diffraction orders. The resonance shown in Fig. 14 corresponds to the $n = +1$ SPW coupling; there is also a propagating $n = -1$ diffraction order throughout this angular range. The numbers labeling the SPW curves in the figure represent the relative intensity of the mode. The results from the present treatment for the same parameters are shown in Figs. 14(b)-14(d). Note the overall similarity of the calculated intensities and line shapes. Interestingly, the largest discrepancy is for the shallowest grating, $h_1 = 0.01$, where

the present calculation yields a SPW intensity that is 24% larger than the more rigorous calculation of Garcia.³⁸ For deeper gratings the agreement is generally within 10%. A similar result was found by Weber³⁴ in his development of a coupled-mode analysis. This comparison indicates that despite the relative simplicity of the formulation the present model provides substantial insight into SPW coupling.

COMPARISON OF THEORY AND EXPERIMENT

The initial step in a comparison of this model with the experimental results is the establishment of the deposition-dependent dielectric properties of the Ag films. Various values of the Ag dielectric constant at a 633-nm wavelength have been reported, viz., $(-16.4, 0.54)$,³⁹ $(-17.9, 0.49)$,⁴⁰ and $(-18.9, 2.35)$.⁴¹ As is reflected in this wide dispersion of reported values, the dielectric properties of thin films are dependent on deposition- and substrate-dependent columnar structure, granularity, subideal density, and incorporated impurities. Given this uncertainty, the approach adopted here is to adjust the dielectric properties to obtain a best fit to the experimental result for a single grating [510-nm period, 22-nm depth; Fig. 2(c)], which gives a value of $(-13.65, 0.82)$; this value was used for all the comparisons between theory and experiment. The fit for this grating is shown in Fig. 15; excellent agreement is obtained for a calculated depth of 19 nm. In subsequent measurements, which will be reported in detail elsewhere, the dielectric properties of Ag films deposited on Si substrates under identical conditions were determined independently by ellipsometric techniques to be $(-12.9, 0.76)$, within 7% of the values obtained here. The grating fabrication and the film deposition involved in the present study were carried out over a period of several months, and deposition conditions and the resulting film properties invariably drift over this time period; no adjustment was made in the dielectric values used in the comparison between theory and experiment.

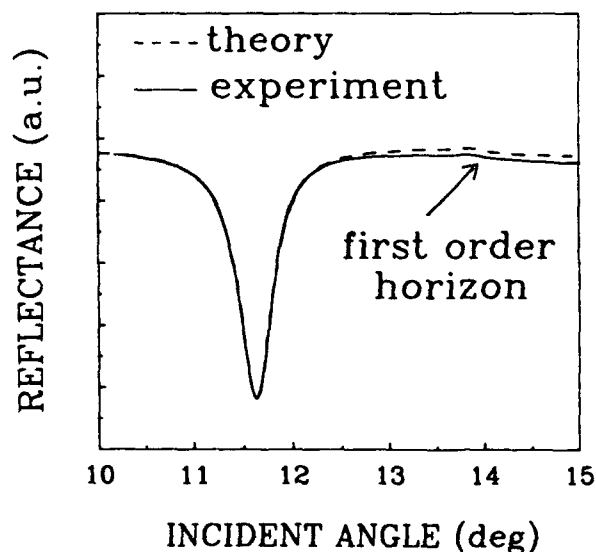


Fig. 15. Calculated zero-order reflectivity SPW resonance line shapes for $\epsilon = (-13.65, 0.82)$ at grating depth $h = 19$ nm. The experimental result ($h = 22$ nm) is shown as the solid curve.

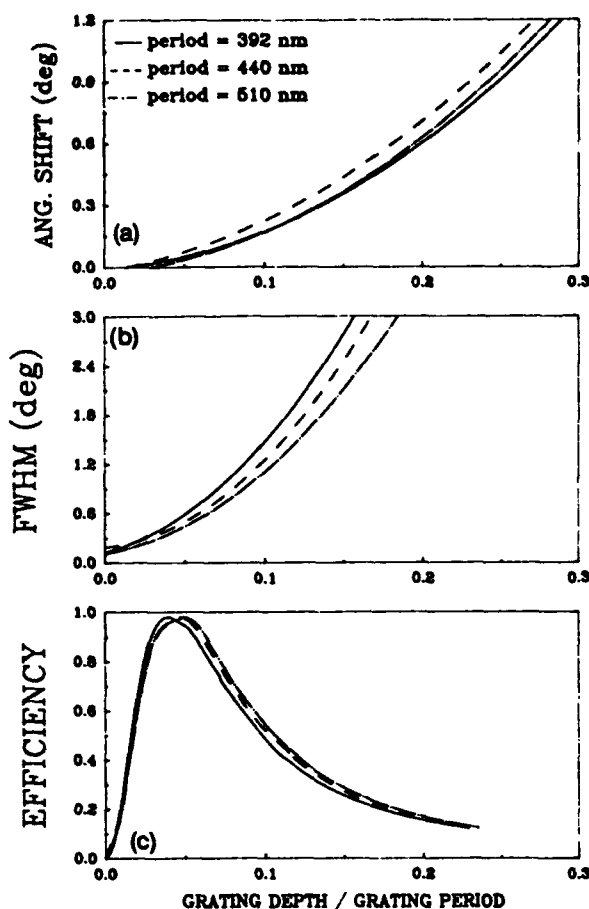


Fig. 16. Calculated SPW resonance parameters plotted against the dimensionless parameter h/d .

Comparisons with the experimental results are shown on the right-hand sides of Figs. 2 and 3. In each case the grating depth for the calculation is adjusted to give coupling efficiencies that match the experimental results. There is overall excellent agreement. For the deepest grating shown experimentally, $h = 145$ nm, there is a substantial difference with the model that is probably associated with the significant deviation from a simple sinusoidal profile at this depth (cf. Fig. 4). Figures 5–7 present the model results along with the experimental data for the coupling efficiency, the resonance angle, and the resonance linewidth for all three grating periods investigated. There is an excellent qualitative match between theory and experiment. The most significant deviation, that for the linewidth of the 440-nm-period gratings, is most probably due to a variation in the film dielectric properties for this set of gratings. The coupling efficiencies first increase rapidly as the grating depth is increased, saturate near 100% coupling, and then decrease as the resonance becomes overcoupled owing to radiative damping back into the zero-order radiation fields. This coupling change is accompanied by approximately quadratic changes in the resonance angle and linewidth with increasing grating depth. Remarkably similar qualitative behavior was predicted by Weber and Mills²¹ in their numerical analysis of grating coupling for 800-nm-period Ag sawtooth gratings. They evaluated the third-order

coupling at $\lambda = 480$ nm and found a maximum coupling strength for grating depths of 40–60 nm.

The model results are summarized in Fig. 16, which shows the calculated resonance angle, resonance linewidth, and coupling strength plotted against the dimensionless parameter h/d for the three grating periods investigated. For evaluation of the coupling efficiency this parameter is reasonably invariant; there are more significant deviations in the evaluation of the resonance line-shape parameters.

Overall, this simple model provides a good picture of the experimentally observed resonance variations. Disagreements between theory and experiment increase for deeper gratings and larger periods. A significant phenomenon not included in the theoretical model is the deviation from sinusoidal grating profiles, which increases as the grating depth is increased and also is more significant for larger grating periods. The films also exhibit significant surface roughness (see Fig. 4), which has not been included in the model and may influence the observed line shapes.

Calculated zero-order, TM-polarization reflectivity curves for deeper gratings, up to $h/d \sim 1$, are shown in Fig. 17. Again, there is good qualitative agreement with the large coupling into the diffraction order for deep gratings ($h/d \sim 0.5$), although detailed comparisons are not possible because of the strong deviation from a simple sinusoidal profile of the experimental gratings. The model does not show the absorption of TM-polarized radiation seen experimentally. A detailed comparison with experiment requires deep sinusoidal gratings, which are inherently difficult to fabricate because of the strong nonlinearities of existing photoresists.²⁷ More nearly sinusoidal gratings can be fabricated on a transparent substrate; research continues in the pursuit of a better experimental test of the model for deep gratings. The theoretical model loses much of its simplicity for rectangular gratings, where many Fourier components of the grating profile are comparable in intensity.

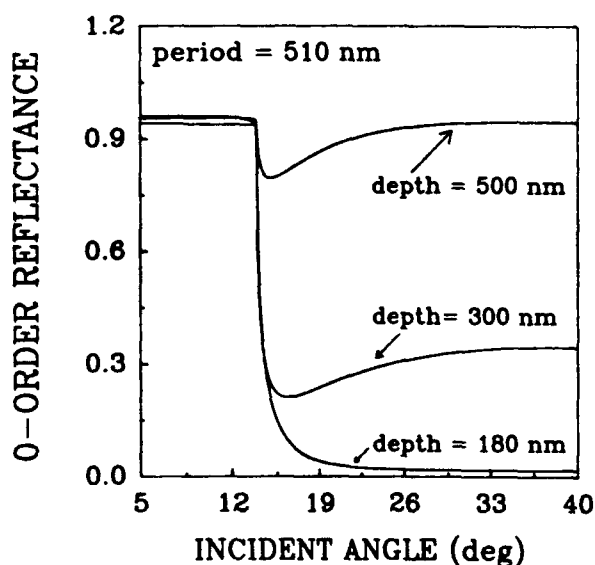


Fig. 17. Calculated zero-order reflectivity for deep ($h/d \sim 1$) sinusoidal gratings in TM polarization ($d = 510$ nm).

SUMMARY

A systematic experimental and theoretical study of first-order grating coupling to SPW's existing at an air-Ag interface was reported. The experiment extends the range of investigated grating depths to $h/d \sim 1$. For TM-polarized incident radiation this includes the entire range of SPW-radiation coupling—from underdamped, to nearly 100% coupling, to overdamped and the ultimate disappearance of the SPW resonance from the observed zero-order reflectance. Strong polarization and absorption effects are observed for the deepest gratings. A simple theoretical model, based on the Rayleigh hypothesis and retaining only resonant diffraction terms without making a small-signal approximation, provides good agreement with the experimental results.

Several extensions of this work are immediately apparent. For larger grating periods there are more diffraction orders and SPW coupling resonances. Interesting coupling effects occur when two of these resonances occur at approximately the same angle. These effects have been investigated experimentally and theoretically and will be reported in a subsequent publication. In addition, the SPW resonance can be used to characterize metal optical constants under a variety of deposition conditions. A study is under way that compares this technique with more conventional techniques such as ellipsometry.

ACKNOWLEDGMENT

This research was partially supported by the U.S. Air Force Office of Scientific Research.

S. R. J. Brueck is also with the Departments of Electrical Engineering and Physics, University of New Mexico, Albuquerque, New Mexico 87131.

*Present address, Electronics Division, PINSTECH, P. O. Box Nilore, Islamabad, Pakistan.

REFERENCES

1. R. W. Wood, *Philos. Mag.* **4**, 396 (1902).
2. Lord Rayleigh, *Philos. Mag.* **14**, 60 (1907).
3. Lord Rayleigh, *Proc. R. Soc. London Ser. A* **79**, 399 (1907).
4. U. Fano, *J. Opt. Soc. Am.* **31**, 213 (1941).
5. A. Sommerfeld, *Ann. Phys. (Leipzig)* **28**, 665 (1909).
6. A. D. Boardman, ed., *Electromagnetic Surface Modes* (Wiley, New York, 1982).
7. E. A. Stern, as quoted in R. A. Ferrel, *Phys. Rev.* **111**, 1214 (1958).
8. Y. Y. Teng and E. A. Stern, *Phys. Rev. Lett.* **19**, 511 (1967).
9. J. J. Cowan and E. T. Arakawa, *Z. Phys.* **235**, 97 (1970).
10. M. C. Hutley, *Opt. Acta* **20**, 607 (1973).
11. M. C. Hutley and V. M. Bird, *Opt. Acta* **20**, 771 (1973).
12. M. C. Hutley and D. Maystre, *Opt. Commun.* **19**, 431 (1976).
13. R. Petit, ed., *Electromagnetic Theory of Gratings* (Springer-Verlag, Berlin, 1980).
14. I. Pockrand, *Phys. Lett. A* **49**, 259 (1974).
15. I. Pockrand and H. Raether, *Opt. Commun.* **18**, 395 (1976).
16. I. Pockrand, *J. Phys. D* **9**, 2423 (1976).
17. I. Pockrand and H. Raether, *Appl. Opt.* **16**, 1784 (1977).
18. H. Raether, *Opt. Commun.* **42**, 217 (1982).
19. E. Kroger and E. Kretschmann, *Phys. Status Solidi B* **76**, 515 (1976).
20. V. M. Agranovich and D. L. Mills, eds., *Surface Polaritons* (North-Holland, Amsterdam, 1982).
21. M. Weber and D. L. Mills, *Phys. Rev. B* **27**, 2698 (1983).
22. F. Toigo, A. Marvin, V. Celli, and N. R. Hill, *Phys. Rev. B* **15**, 5618 (1977).
23. N. E. Glass, M. Weber, and D. L. Mills, *Phys. Rev. B* **29**, 6548 (1984).
24. M. G. Weber, *Phys. Rev. B* **33**, 909 (1986).
25. M. Yamashita and M. Tsuji, *J. Phys. Soc. Jpn.* **52**, 2462 (1983).
26. S. D. Gupta, G. V. Varada, and G. S. Agarwal, *Phys. Rev. B* **36**, 6331 (1987).
27. S. H. Zaidi and S. R. J. Brueck, *Appl. Opt.* **27**, 2999 (1988).
28. J. L. Roumiguieres, D. Maystre, and R. Petit, *J. Opt. Soc. Am.* **67**, 557 (1977).
29. J. L. Roumiguieres, *Opt. Commun.* **19**, 76 (1976).
30. K. Knop, *Opt. Commun.* **26**, 28 (1978).
31. K. Utagawa, *J. Opt. Soc. Am.* **69**, 333 (1979).
32. M. Naviere, P. Vincent, R. Petit, and M. Cadilhac, *Opt. Commun.* **9**, 48 (1973).
33. H. Numata, *J. Phys. Soc. Jpn.* **51**, 2575 (1982).
34. S. S. Jha, J. R. Kirtley, and J. C. Tsang, *Phys. Rev. B* **22**, 3973 (1980).
35. P. M. Van den Berg and J. T. Fokkema, *J. Opt. Soc. Am.* **69**, 27 (1979).
36. R. Petit and M. Cadilhac, *C. R. Acad. Sci.* **262**, 468 (1966).
37. T. C. Paulick, *Phys. Rev. B* **42**, 2801 (1990).
38. N. Garcia, *Opt. Commun.* **45**, 307 (1983).
39. G. P. Motulevich, *Optical Properties of Metals* (Consultants Bureau, New York, 1973).
40. P. B. Johnson and R. W. Christy, *Phys. Rev. B* **6**, 4370 (1972).
41. R. Weast and D. Lide, eds., *Handbook of Physics and Chemistry*, 70th ed. (CRC, Boca Raton, Fla., 1989).

Grating coupling to surface plasma waves.

II. Interactions between first- and second-order coupling

Saleem H. Zaidi, M. Yousaf,* and S. R. J. Brueck

Center for High Technology Materials, University of New Mexico, Albuquerque, New Mexico 87131

Received May 17, 1990; accepted November 26, 1990; manuscript in hand January 25, 1991

For grating periods larger than the excitation wavelength, multiple-grating orders couple incident optical radiation to the surface plasma waves (SPW's) characteristic of the metal-air interface. For a grating period that is an integral multiple of the wave vector of these surface modes, two resonances become degenerate in coupling angle. There are also permitted diffraction orders at this coupling angle. The vicinity of this multiple-mode coupling resonance, where several free-space electromagnetic modes, as well as two surface modes, are coupled by different orders of a grating, is known as a minigap region. Not surprisingly, the response surface displays complex dependences on frequency, angle, and grating profile. A detailed experimental and theoretical study is presented of the optical response at 633 nm in the $(+1, -2)$ minigap region for Ag films deposited on photolithographically defined 870-nm-period gratings. Measurements of both the 0-order reflectance and the -1 -order diffraction are presented for a wide progression of grating depths. The SPW resonances depend on the grating depth, and this variation is used to tune through the minigap region for a fixed wavelength and period. Similar measurements are presented for a single grating as a function of wavelength through the minigap region. In both measurements the 0-order response shows only a single broad minimum as the resonances approach degeneracy, while the -1 -order diffraction shows clearly defined momentum gaps. A simple theoretical model based on the Rayleigh hypothesis is presented that gives a good qualitative picture of the response. The response surfaces are sensitive to the grating profile, and detailed modeling requires inclusion of higher-order grating components.

1. INTRODUCTION

Optical interactions with metallic gratings have long fascinated scientists. Wood's initial observations of grating anomalies¹ were classified by Fano² into (1) diffraction anomalies associated with the redistribution of energy among diffraction orders when one order passes over the horizon (i.e., the propagation direction reaches an angle of 90° to the grating normal) and (2) resonance anomalies associated with the propagation of guided waves along the grating interface. A large body of experimental and theoretical research relating to optical interactions with periodic surfaces has been accumulated.^{3,4} This paper is concerned with resonance anomalies and is focused on the propagation of guided waves, known as surface plasma waves (SPW's), on bare metallic surfaces.

For grating periods less than the excitation wavelength, only first-order coupling to SPW's is permitted and has been described in detail elsewhere.⁵ For grating periods larger than the incident wavelength it is possible to couple to SPW's in higher orders and to observe electromagnetic interactions between these couplings. These interactions are the major focus of this paper. The first experimental evidence of these interactions between different coupling orders was provided by Stewart and Gallaway,⁶ who observed that in some cases Wood's anomalies did not become coincident but repelled each other as the optical wavelength was varied to bring the resonances closer together. Ritchie *et al.*⁷ also observed gaps in the dispersion relation of the SPW's and attributed them to higher-order interactions between SPW's. Hutley⁸ and Hutley and Bird⁹ car-

ried out a detailed experimental study of the anomalies of sinusoidal diffraction gratings in the visible spectrum. The anomalies were characterized in a Littrow configuration as a function of groove depth, period, and wavelength, and in some cases a reluctance of anomalies to merge was observed. Kroo *et al.*¹⁰ observed similar gaps in the dispersion relation of SPW's in metal-oxide-metal structures and attributed them to the crossing of $(+1, -1)$ coupling to SPW's. Chen *et al.*¹¹ experimentally investigated grating coupling to SPW's in the minigap regions, i.e., degenerate coupling to SPW's in two different grating orders, such as $(+1, -2)$ or $(+2, -2)$, and measured energy gaps for various minigap regions. Weber and Mills¹² and Tran *et al.*¹³ showed theoretically that interactions of elastically scattered SPW's result in complex response surfaces in the vicinity of the minigaps and that a direct interpretation in terms of a modal dispersion relation is difficult at best. Detailed modeling and careful evaluation of couplings in both amplitude and phase are necessary for a full appreciation of the experimental results. Heitman *et al.*¹⁴ showed from experimental studies on metal-oxide-metal structures that the existence of energy or momentum gaps was dependent on the mode of excitation and the experimental observable; i.e., using fast electron excitation and light emitted from metal-oxide-metal structures, they observed energy and momentum gaps, but only energy gaps were observed from optical excitation (similar to Chen's results). They also pointed out that the anomalies strongly depend on grating period, depth, and profile as well as on the excitation mechanism and the method of detection.

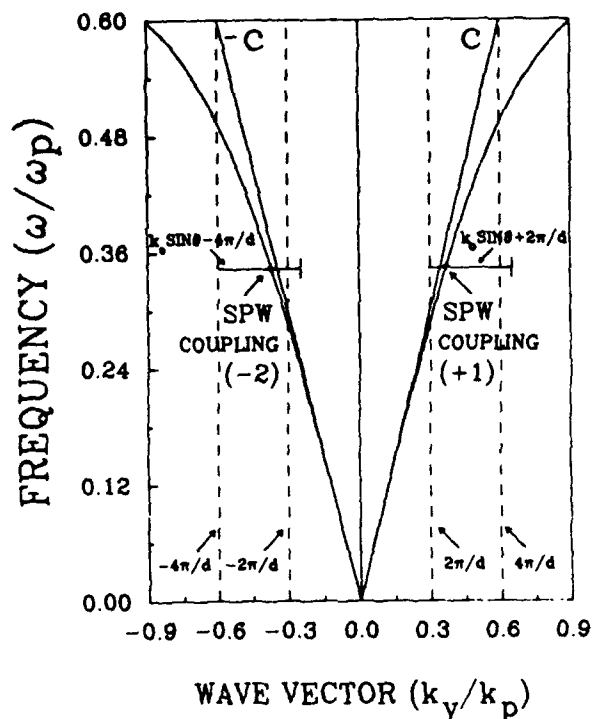


Fig. 1. Dispersion relation of SPW's for a lossless, free-electron metal ($\epsilon = 1 - \omega_p^2/\omega^2$). The axes are normalized to ω_p and $k_p = \omega_p/c$. The grating vectors corresponding to the $n = \pm 1$ and $n = \pm 2$ orders of a grating of period d are shown as vertical dashed lines. The range of wave vectors accessible by varying the input angle from normal to grazing incidence for $n = +1$ and $n = -2$ is shown as horizontal lines. Note that for this choice of parameters ($\lambda/d = 0.73$), there are two SPW resonances and that the -1 diffraction order propagates throughout the angular range.

When higher-order couplings to SPW's are studied, the permitted diffraction orders are strongly coupled to the SPW's; therefore the incident beam, all propagating diffracted beams, and the SPW's must be taken into account for a complete understanding of these complex interactions. The effect of SPW resonance on diffraction orders has been studied by many authors.¹⁵⁻¹⁷ However, all those studies dealt with single SPW resonance; the effects of multiple couplings have not been investigated experimentally. Here, a systematic theoretical and experimental investigation of SPW interference in the $(+1, -2)$ minigap region is presented. Both the 0-order reflectance and the -1 -order diffraction (the only permitted diffraction order in the angular region of SPW coupling) were measured at 633 nm as a function of the incident angle for various grating depths and profiles at a fixed grating period of 870 nm. The angular shifts in the SPW resonance angles as a result of the increasing grating depths were used to tune through the coupling degeneracy. By adding intensities in the 0-order reflectance and the -1 -order diffraction to find the total reflected energy, we observed momentum gaps. Also, for a single-grating profile similar measurements were repeated as a function of wavelength. Consistent with the experimental results discussed above, momentum gaps were not found in the 0-order reflectance; however, well-defined momentum gaps were observed in the -1 diffraction order.

Finally, a simplified theoretical formalism, developed for the analysis of first-order coupling,⁶ is extended. This

analysis, based on a simple truncation of the plane-wave expansion of the scattered fields within the Rayleigh hypothesis, provided remarkably good agreement with the first-order coupling results. Not surprisingly, while the major features of the experiment are reproduced, the agreement is less satisfactory for this more demanding case.

The dispersion relation for SPW's at a metal-air interface is given by¹⁸

$$k_{\text{SPW}} = k_0 [\epsilon/(1 + \epsilon)]^{1/2}, \quad (1)$$

where k_0 is the free-space propagation vector and ϵ is the metal dielectric constant. The excitation of SPW's takes place whenever the wave vector of the incident light parallel to the metal-air grating interface satisfies the condition

$$k_0 \sin \theta + 2\pi n/d = \pm k_{\text{SPW}}, \quad (2)$$

where θ is the incident angle, d is the grating period, and $n = 0, \pm 1, \pm 2, \dots$ represents the coupling order. For a lossless free-electron metal ($\epsilon = 1 - \omega_p^2/\omega^2$), the dispersion relation [Eq. (1)] is plotted in Fig. 1, where $k_p = \omega_p/c$. The vertical dashed lines represent the various grating orders, and the horizontal lines indicate the accessible wave vectors ($2\pi n/d$ to $k_0 + 2\pi n/d$) in the $+1$ and -2 orders. Note that coupling to SPW's can be achieved for both of these orders for the choice of ω and d corresponding to the present experiment. Coupling in the $+1$ (-2) orders results in the propagation of SPW's in the forward (backward) [i.e., same (opposite)] direction as the y component of the incident wave vector. The -1 diffraction order is permitted throughout the angular range of the two SPW couplings, and its properties are strongly influenced by the SPW resonances. Also note that degeneracy in the coupling angle θ corresponds to the coupling of the oppositely directed SPW's by an integral multiple of the grating wave vector (3 in this case). In a fashion familiar from many examples of mode coupling, this degeneracy results in the interactions between the SPW modes that give rise to the minigap effects.

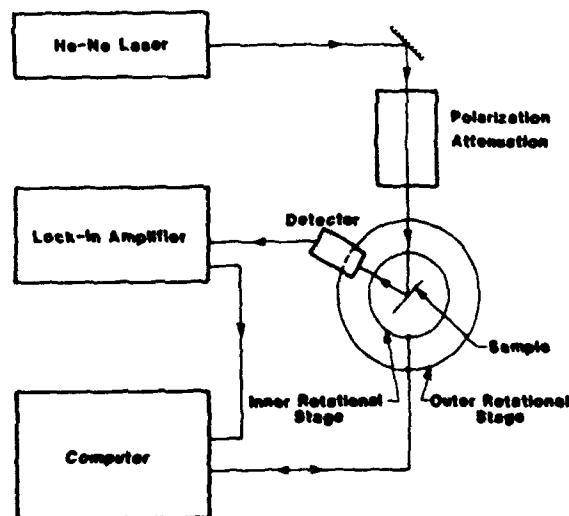


Fig. 2. Experimental arrangement for reflection and diffraction-order measurements.

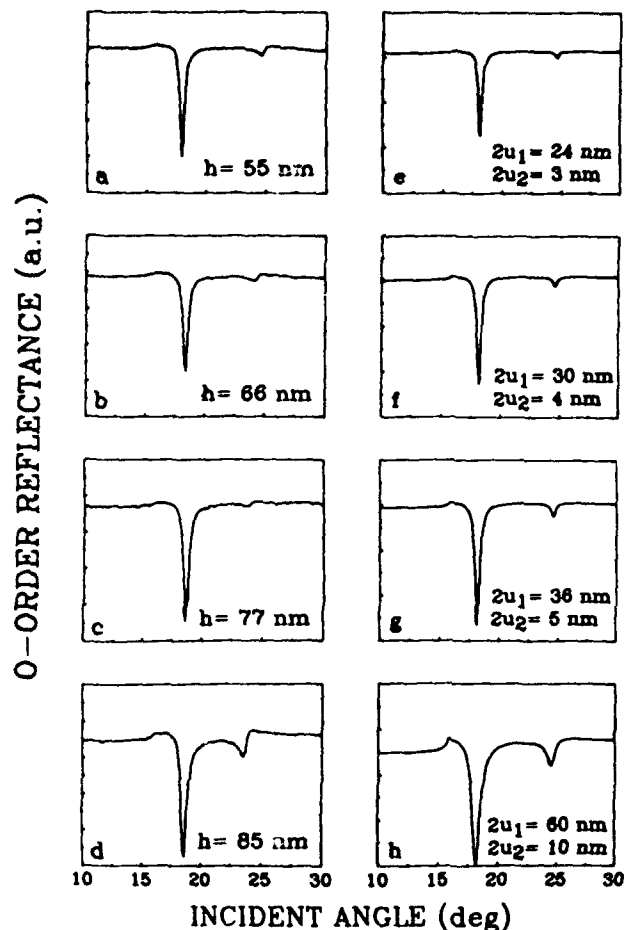


Fig. 3. 0-order reflectances at 633 nm for 870-nm-period gratings with varying grating depths h . The left-hand column presents experimental results; the right-hand column presents theoretical modeling. See the text for details.

2. EXPERIMENT

Gratings were fabricated holographically in positive photoresist on Si substrates with a single-frequency Ar-ion laser source at 488 nm.¹⁹ Grating depths were varied by adjustment of the exposure time. This results in variations in both the depth and the grating profile, which varies from approximately sinusoidal at small depths to rectangular at the deepest gratings investigated. These photoresist gratings were coated with ~100-nm-thick Ag films with the use of an electron-beam evaporator system at room temperature and at a background vacuum of low- 10^{-6} Torr.

The optical measurements were scans of reflectance (diffraction) versus incident angle in the experimental setup shown in Fig. 2. In this arrangement two concentric rotation stages are used, with the sample mounted on the inner stage and the detector mounted on the outer stage. The data acquisition step involved a personal computer interfaced with a stepper motor controller, which, in turn, controlled the two rotation stages. Most measurements were made at the He-Ne laser wavelength. For the variable-wavelength measurements a cw-dye-laser source was used. Grating depths were measured in cross section with a scanning electron microscope (SEM). This introduces errors, estimated at ± 5 nm, owing to uncertainties in the SEM calibration and to variations in grating depths

for the different areas sampled in the optical and SEM measurements.

3. 0-ORDER REFLECTANCE MEASUREMENTS

Figures 3a–3d show the 0-order reflectance scans as the grating depth is increased. The plots in Figs. 3e–3h are obtained from the modeling and will be discussed in Section 8. The following important features should be noted:

- (1) The excitation of SPW's in the first ($n = +1$) and second ($n = -2$) orders at $\sim 18^\circ$ and 24.7° , respectively,
- (2) The horizon for the associated diffraction orders at 15.8° and 27.1° , respectively,
- (3) The increase in the first-order coupling efficiency as the grating depth is increased,
- (4) The relative weakness of the second-order coupling,
- (5) The decrease in the angular separation of the two coupling resonances as the grating depth is increased.

Also note that the angular shifts in the second-order resonance are almost twice those in the first order.

For deeper gratings the corresponding measurements are shown in Figs. 4a–4d; as before, Figs. 4e–4h are obtained from theory. Note the following features:

- (1) The increase in the -2 -order coupling strength,
- (2) The merging of the first- and second-order couplings, resulting in a saddle-point line shape,

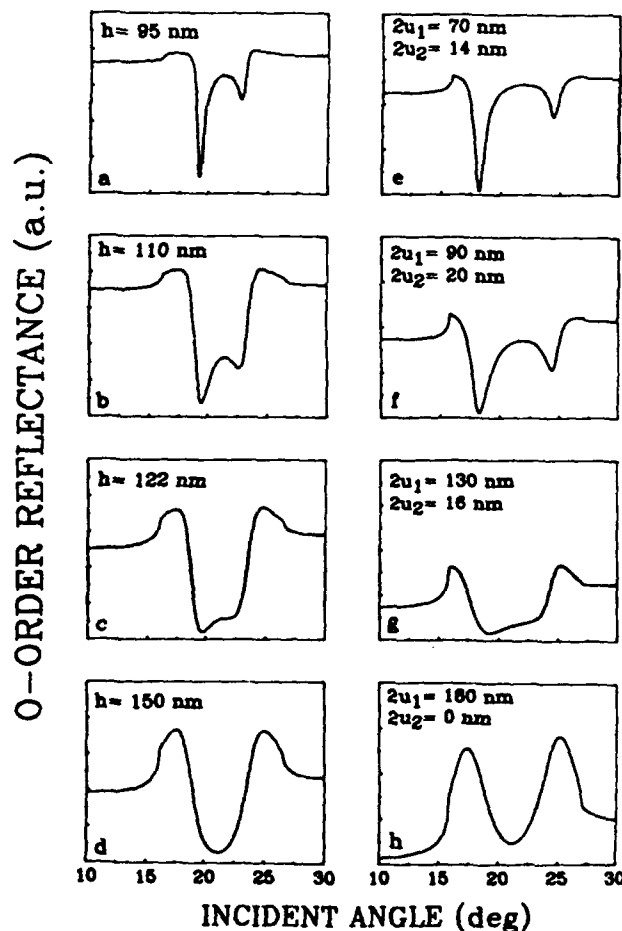


Fig. 4. Same as Fig. 3 but for deeper gratings.

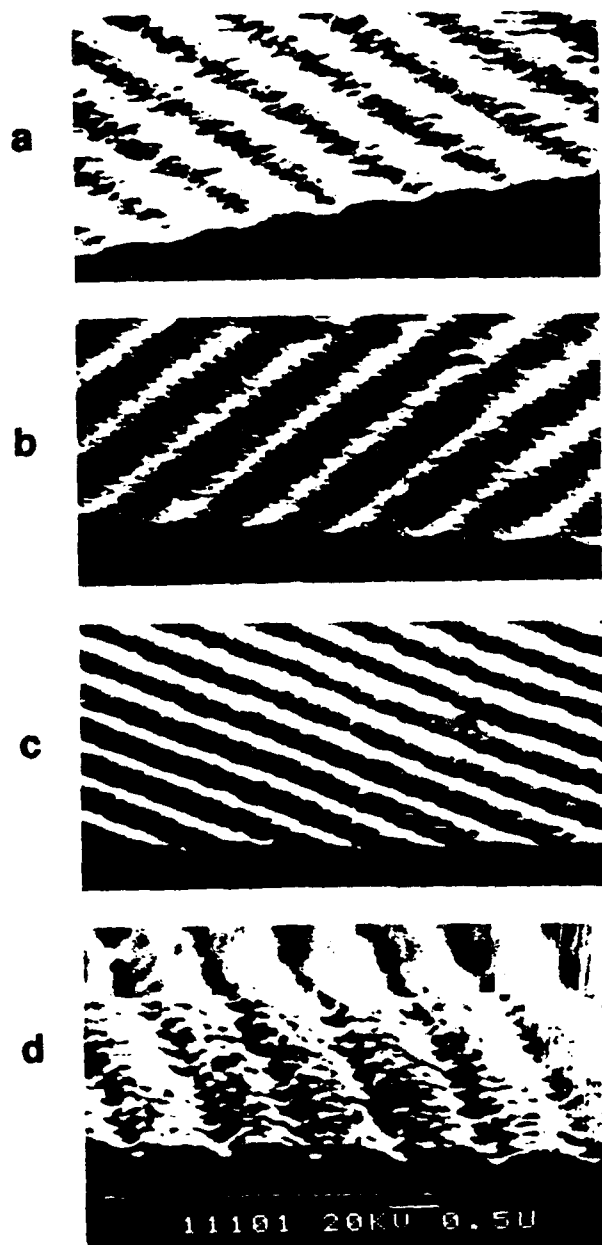


Fig. 5. Cross-section SEM photographs of the gratings used for the experiments. The measured depths are (a) 95 nm, (b) 110 nm, (c) 122 nm, and (d) 150 nm.

(3) The emergence of a broad minimum (Fig. 4d), where first- and second-order couplings can no longer be distinguished.

This is similar to the behavior observed¹¹ and calculated¹² for similar fixed-frequency reflectivity scans in the vicinity of a minigap. As a result of the saddle-point response surface, only a single, broad resonance is observed when θ is varied for fixed ω , while two distinct resonances and an energy gap are found when ω is varied for fixed θ .

In Fig. 5 SEM profiles of the gratings used to obtain Figs. 4a–4d are shown. Increasing grating depth also results in increasing deviation from sinusoidal profiles as a result of the grating fabrication technique.¹³ For still deeper gratings the corresponding measurements are shown in Fig. 6, where the vertical scale is unchanged

from that of Figs. 3 and 4. For these approximately rectangular grating structures (cf. Fig. 7), there is an overall decrease in the 0-order reflectance, an absence of clear SPW coupling resonances, and line shapes that do not lend themselves to simple interpretation.

4. -1-DIFFRACTION-ORDER MEASUREMENTS

For this grating period and measurement wavelength the -1 diffraction order is a propagating mode throughout the entire incident angle range including that of the SPW resonances. Coupling to this propagating order provides additional information on the SPW resonance characteristics. In fact, the first observations of Wood's anomalies were related to diffraction orders rather than to 0-order reflectance. Measurements of the energy coupled into the SPW mode must take into account both the reflectance and the energy coupled into the diffraction order. Diffraction-order scans corresponding to the 0-order scans of Figs. 3a–3d are shown in Figs. 8a–8d; as above, the plots in Figs. 8e–8h are obtained from theory. The vertical scale on these measurements is the same as that for the 0 order, so the diffracted energy in the -1 order is significant when compared with the reflectivity. The following features should be noted:

- (1) The line shapes are derivativelike as the incident angle is varied through the SPW resonances,
- (2) The coupling strengths are equal, in contrast with the much weaker -2-order coupling observed in the reflectivity (cf. Figs. 3a–3d),
- (3) Neither the maxima nor the minima in the diffraction-order intensities correspond to the 0-order minima,
- (4) There is an enhancement of the diffraction-order intensity in the region between the SPW interactions,
- (5) As the grating depths increase, the angular separation between the SPW resonances as measured between

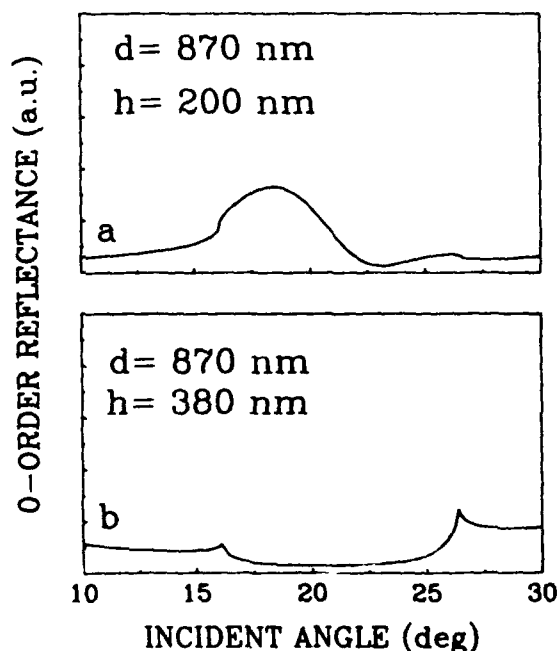


Fig. 6. 0-order reflectances at 633 nm for gratings with (a) residual SPW effects and (b) absorptive behavior.

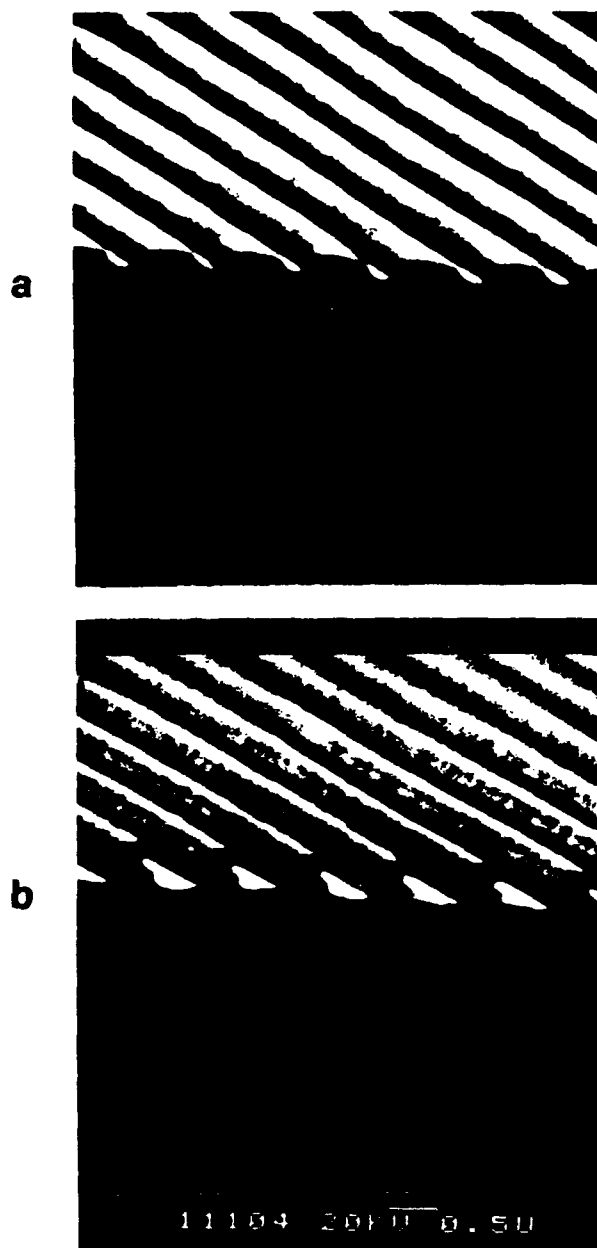


Fig. 7. Cross-section SEM photographs of the gratings used for the measurements in Fig. 6.

either the minima or the maxima of the line shapes first decreases (Figs. 8a–8c) and then increases (Fig. 8d).

For deeper gratings, corresponding to the 0-order scans of Figs. 4a–4d, the diffraction-order scans are shown in Figs. 9a–9d, where, as above, Figs. 9e–9h are the result of theoretical modeling that will be discussed in Section 8. The following features can be noted from these measurements:

- (1) There is an increase in the angular separation of the two minima with increasing grating depth, in contrast with the behavior in the 0-order measurements, where the minima move toward each other and merge,
- (2) There is a decrease in the angular separation of the two maxima (Figs. 9a–9c) and an emergence of a single maximum (Fig. 9d),

(3) The enhancement in the -1 diffraction order is such that the minimum in the 0 order (Fig. 4d) corresponds to the maximum in the diffraction order (Fig. 9d).

A comparison of the 0-order (Figs. 4a–4d) and -1 -diffraction-order (Figs. 9a–9d) measurements shows that much of the incident energy is re-emitted into the diffraction order. This enhancement in the diffraction-order intensity is mediated by SPW interactions.

Finally, the diffraction-order measurements are shown for gratings with residual SPW coupling effects (Fig. 10a) and without SPW effects (Fig. 10b), corresponding to the 0-order scans of Fig. 6. For the shallower grating, there is a decrease in intensity, and two broad minima, at 18.2° and 24° , are observed, with the minimum at 18° corresponding to the maximum in the 0 order (Fig. 6a) and the minimum at 24° corresponding to neither the minimum nor the maximum in the 0 order (Fig. 10a). For the deeper grating measured, there are no residual SPW effects but rather a substantial decrease in the diffraction-order intensity for all angles.

5. ENERGY-SUM MEASUREMENTS

For these measurements, only the 0 and -1 orders are propagating within the angular range of SPW interactions. Thus we can evaluate the total energy coupled to

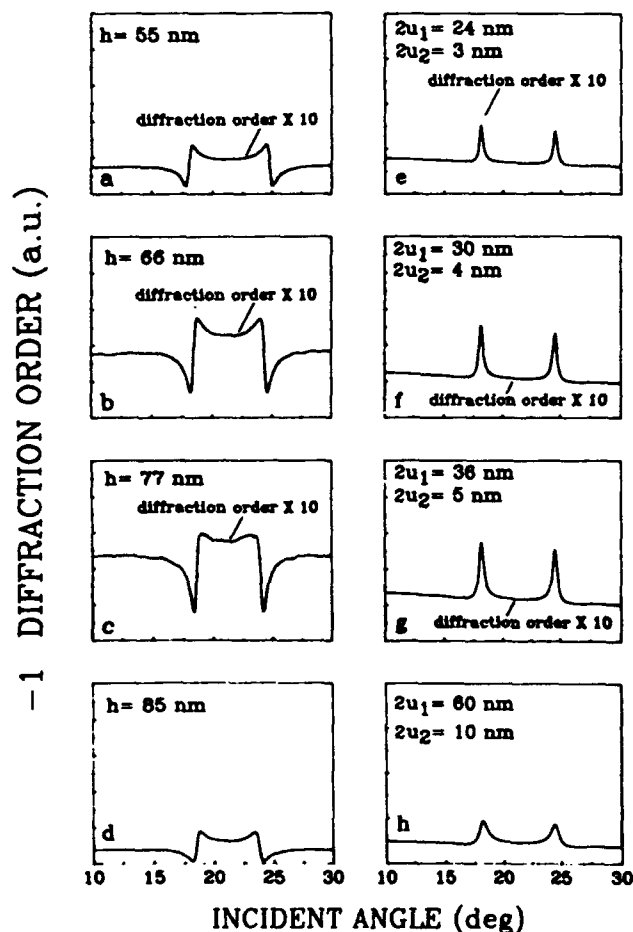


Fig. 8. -1 -diffraction-order scans for the gratings used in Fig. 3. The left-hand column presents experimental results; the right-hand column presents theoretical modeling. See the text for details.

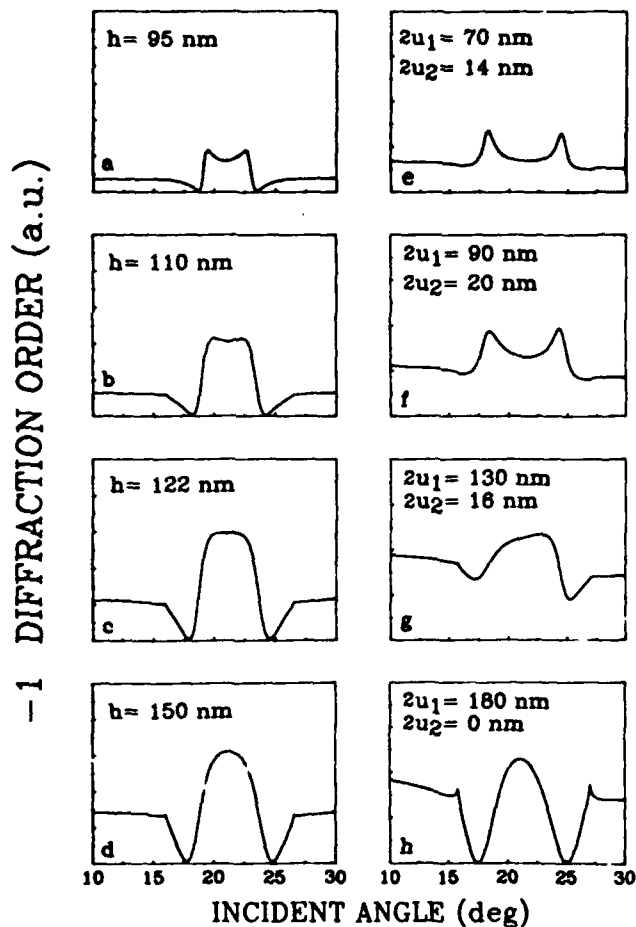


Fig. 9. -1-diffraction-order scans for the gratings in Fig. 4. The left-hand column presents experimental results; the right-hand column presents theoretical modeling. See the text for details.

SPW's by adding the energies in these orders. Figures 11a-11d show these energy sums for the measurements of Fig. 3 (0 order) and Fig. 8 (-1 diffraction order). The measurements for the deeper gratings (Figs. 4 and 9) are given in Figs. 11e-11h. Note that

- (1) The coupling efficiencies are reduced in comparison with the 0 order, since some of the incident energy is also coupled into the diffraction order,
- (2) The coupling of energy to SPW's in the -2 order is manifested by the resonance line shape, in comparison with the less-well-defined line shape of Figs. 3a-3d,
- (3) There is a gradual increase in coupling efficiency and a broadening of the first-order resonance line shape followed by a decreasing efficiency at still deeper gratings,
- (4) There is a decreasing angular separation (Figs. 11a-11f) followed by an increasing separation for deeper gratings.

Both the -1-order measurements and the energy-sum measurements show a well-defined momentum gap; i.e., they show two resonances as a function of θ at fixed ω that first approach each other and then diverge as the grating depth is increased.

The experiments exhibited strong dependence on the details of the grating profiles. For some cases, with approximately sinusoidal profiles, saddle-point line shapes

were not observed in the 0-order reflectances. Also, the diffraction-order line shapes were similar to the 0-order line shapes at SPW resonance angles. Not unexpectedly, the higher-order Fourier components of the grating pro-

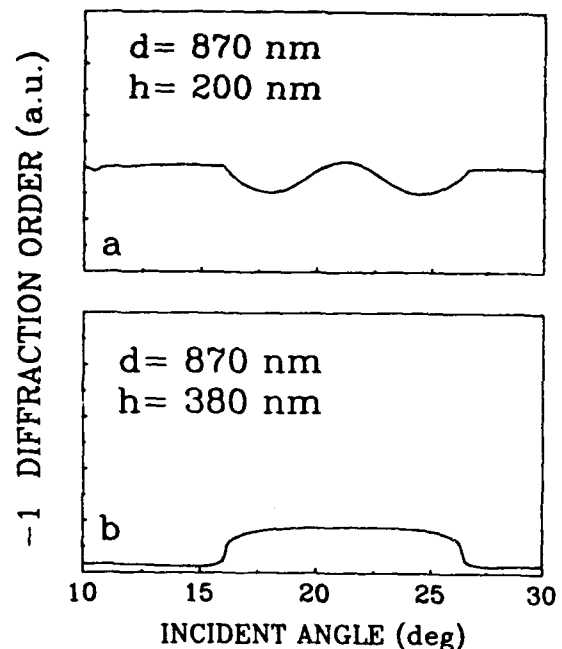


Fig. 10. -1-diffraction-order scans for the gratings used in Fig. 6.

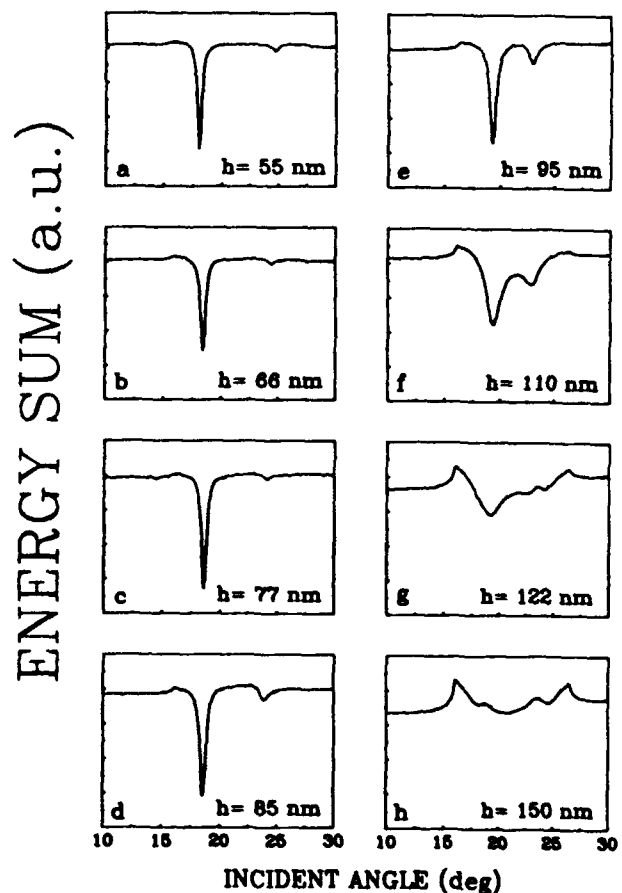


Fig. 11. Energy-sum (0-order reflectance plus -1-diffraction-order) scans for the gratings used in Figs. 3, 4, 8, and 9.

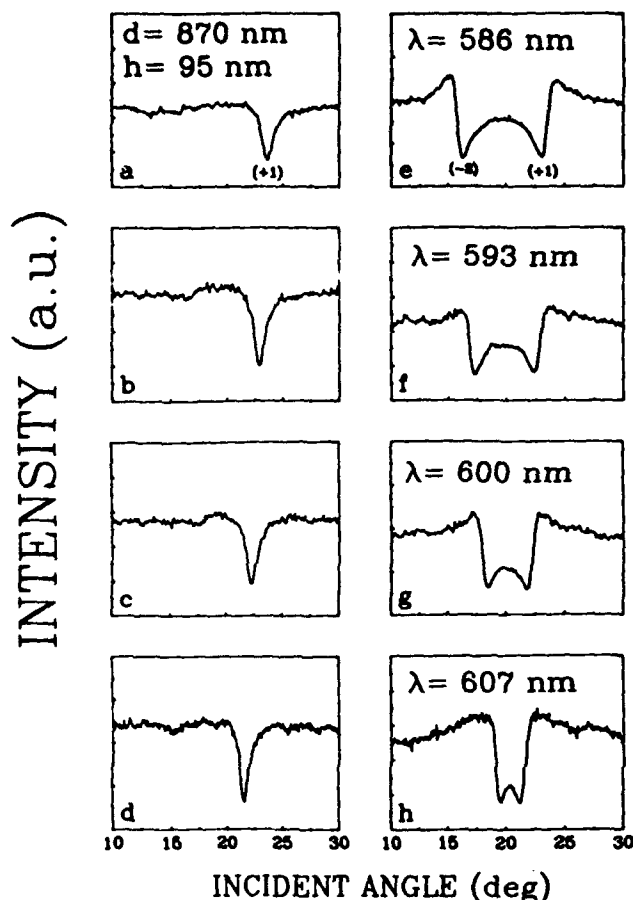


Fig. 12. 0-order reflectance and -1 -diffraction-order scans for the 95-nm-deep gratings (Figs. 4a, 9a, and 11e) as the wavelength is increased from 586 to 607 nm. The left-hand column presents the 0-order measurements; the right-hand column presents the -1 -diffraction-order measurements.

files substantially affect the first- and second-order coupling strengths and line shapes.

6. VARIABLE-WAVELENGTH MEASUREMENTS

For the 95-nm-deep grating (Figs. 4a, 9a, and 11e), a series of 0-order reflectance and -1 -diffraction-order measurements was carried out as a function of wavelength. The output from a dye laser was tuned through the 580–633-nm range, sufficient to probe the $(+1, -2)$ minigap region.

Figure 12 shows the 0-order reflectance (Figs. 12a–12d) and -1 -diffraction-order (Figs. 12e–12h) scans as wavelength is increased from 586 to 607 nm; the vertical scale for the diffraction-order measurements is ten times more sensitive than the corresponding scale for the 0-order measurements. Note the following essential features:

- (1) The angular separation decreases between the $n = +1$ and $n = -2$ couplings, with the angular shifts in the second order being almost twice those in the first order,
- (2) A well-defined resonance is absent in the 0-order scans corresponding to the $n = -2$ coupling, and the broad SPW resonance corresponding to the $n = +1$ coupling moves toward smaller angular values (Figs. 12a–12d),
- (3) The intensity in the -1 diffraction order is gradually reduced in the angular region between the two couplings,

(4) As in the previous measurements, the -1 -diffraction-order measurements show comparable, mirror-image couplings for the two SPW resonances, while the -2 -order coupling is barely observable in the 0-order reflection.

A further increase in wavelength brings the two couplings still closer, and some interference effects are observed as shown in Fig. 13. The major features are the following:

- (1) The monotonic shift to smaller angular values in the 0-order reflectance scans corresponding to the $n = +1$ coupling as the wavelength is changed (Figs. 13a–13d),
- (2) The appearance of a sharp feature at 23.8° in the -1 -diffraction-order measurements (Figs. 13e–13f), which corresponds approximately to the horizon for the appearance of the -2 diffraction order,
- (3) The appearance of a slight discontinuity in the -1 -diffraction-order line shape (Fig. 13g),
- (4) The decrease in the angular separation between the two couplings (Figs. 13e–13g),
- (5) The sharp increase in the diffraction-order intensity as the two couplings cross each other.

In Fig. 14 these measurements are extended to still longer wavelengths, beyond the $(+1, -2)$ minigap region. The major features include

- (1) The appearance of $n = -2$ coupling in the 0-order scans (Figs. 14a–14d),

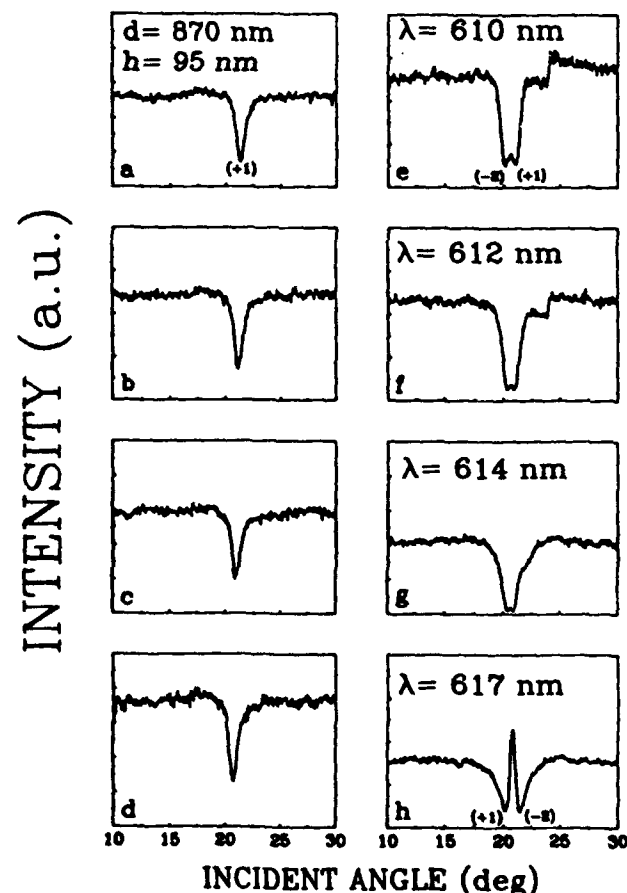


Fig. 13. Same as Fig. 12 but for an increase in wavelength from 610 to 617 nm.

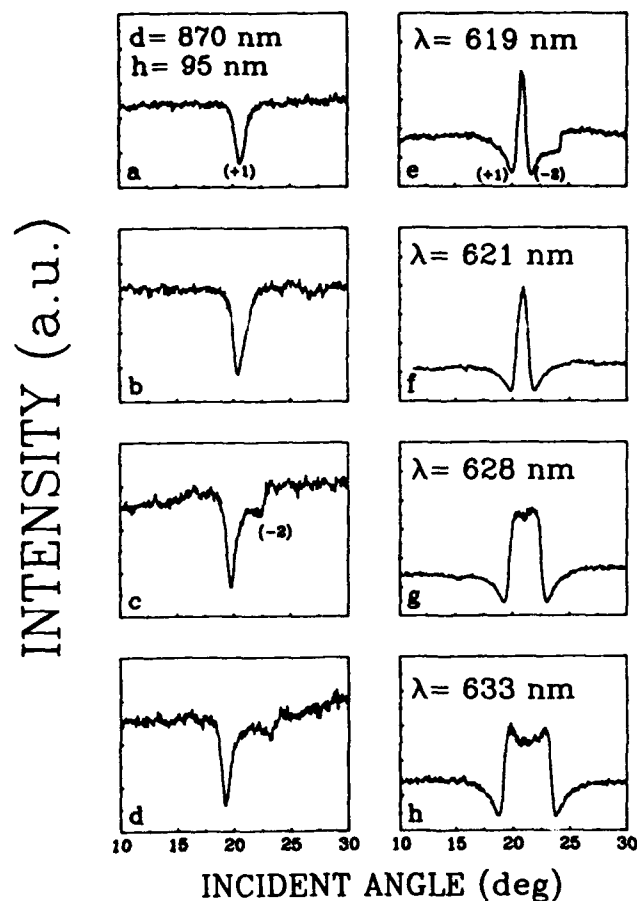


Fig. 14. Same as Fig. 12 but for an increase in wavelength from 619 to 633 nm.

(2) The appearance of a sharp feature at 24.2° (Fig. 14e) corresponding to similar features in Figs. 13e–13f,

(3) The increase in angular separation between the $n = +1$ and $n = -2$ couplings,

(4) The increase in -1 -diffraction-order intensity in the region between SPW couplings,

(5) The reversal of the resonance line shapes in the diffraction-order measurements, evident from a comparison of Figs. 12e–12g and 14e–14g.

Thus, as couplings to SPW's in the first and second orders become degenerate, interference effects result in an enhancement in the diffraction-order intensity over a narrow angular range. When the modes cross each other, the resonances observed in 0 order show a single minimum and do not exhibit a momentum gap (Fig. 15a), while a clearly defined forbidden momentum gap is observed for the -1 -diffraction-order scans (Fig. 15b). The magnitude of this gap is $\sim 0.3^\circ$ and is in good qualitative agreement with the momentum gaps observed by Heitman et al.¹⁴

7. THEORY

A variety of mathematical formalisms have been applied to describe optical interactions with periodic surfaces. Integral methods were first proposed by Petit and Cadilhac,²⁰ Wirgin,²¹ and Uretski.²² A number of integral formulations have been investigated, including a Green's-function formalism based on an extinction theorem mechanism developed by Glass et al.,²³ Laks et al.,²⁴ and Utagawa.²⁵

In addition, differential formalisms developed by Nevière et al.²⁶ and Numata²⁷ have also been used to study SPW dispersion relations. All these methods are rigorous, hold for arbitrary grating profiles, and require extensive computation.

Simpler, approximate formulations have been introduced starting from the Rayleigh hypothesis^{2,28} and from the extinction theorem formalism.²⁹ These were demonstrated to offer a good approximation of the exact calculation²⁹ and to first-order coupling experiments.⁶ While these formulations are lacking in ultimate rigor and accuracy, they offer a good intuitive physical picture of the interaction with a minimum of computational difficulty. Here, the extension of this simple formulation for the minigap region is briefly described. More details are presented in Appendix A.

For TM-polarized light incident on a sinusoidal surface with an excursion of $2u$, a straightforward but involved algebraic procedure results in the coupled linear differential equations

$$J_p(k, u) + \sum_n B_n^* (-1)^{p-n} J_{p-n}(\alpha_n u) - \sum_n B_n^* J_{p-n}(\beta_n u) = 0, \quad (3)$$

$$\begin{aligned} & \left(K_z - pg \frac{k_0}{k_z} \right) J_p(k, u) \\ & - \sum_n \left[\alpha_n - (p-n)g \frac{k_n}{\alpha_n} \right] B_n^* (-1)^{p-n} J_{p-n}(\alpha_n u) \\ & - \frac{1}{\epsilon} \sum_n \left[\beta_n - (p-n)g \frac{k_n}{\beta_n} \right] B_n^* J_{p-n}(\beta_n u) = 0, \quad (4) \end{aligned}$$

where all variables are defined in Appendix A.

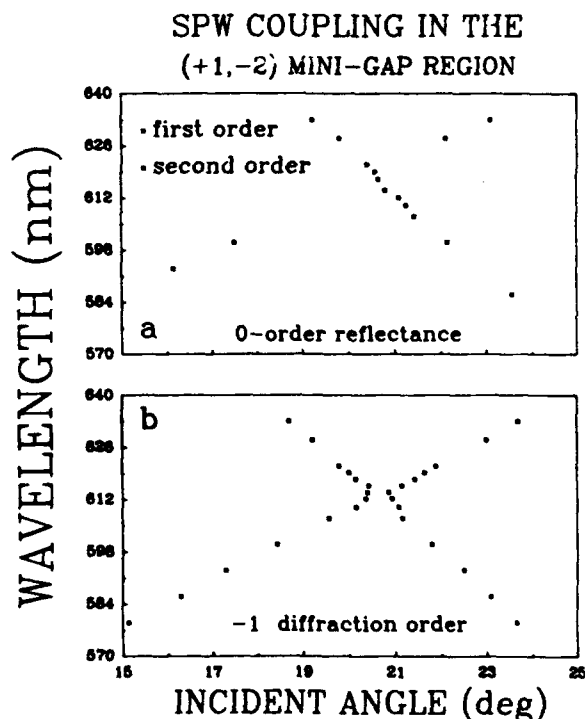


Fig. 15. Plot of the resonance behavior observed in Figs. 12–14. The 0-order reflectivity (a) shows a single dominant resonance becoming a single broad minimum in the minigap region. In contrast, the -1 -diffraction-order scans (b) show a well-defined momentum gap corresponding to the $(+1, -2)$ minigap region.

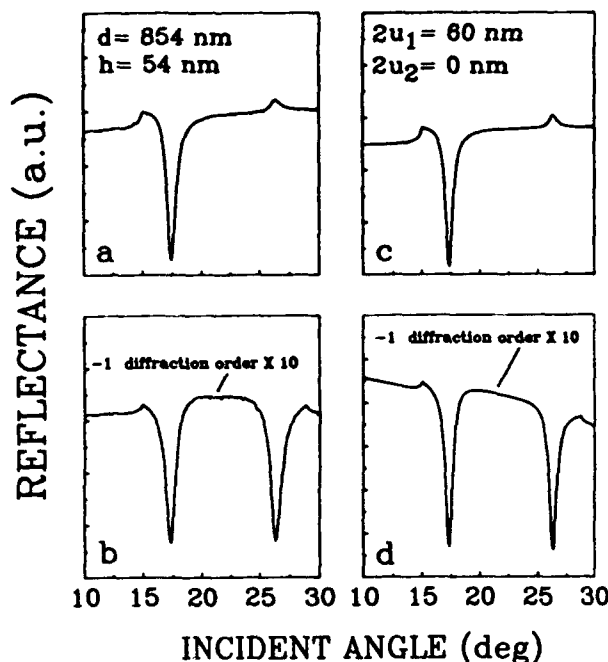


Fig. 16. Comparison between theory and experiment for a grating with a nearly sinusoidal profile. The left-hand column presents experimental results; the right-hand column presents theoretical modeling.

In the derivation of Eqs. (3) and (4) no small-signal approximation is made for either the grating depth or the diffraction-order amplitudes. From the dispersion-relation curve in Fig. 1, for the present case the only resonant terms in the above expansions [Eqs. (3) and (4)] are $n = +1$ and $n = -2$. The $n = -1$ term is the permitted diffraction order and is strongly influenced by SPW interactions. The infinite series was truncated at $n = 0, -1, 1, -2$, which resulted in an 8×8 matrix and considerable simplification. Previous analyses included many more terms and provided significantly greater accuracy. Since the experimental profiles were not precisely sinusoidal, additional Fourier components were included in the grating profile. It was shown by Van den Berg and Fokkema²⁰ that the Rayleigh hypothesis would still be valid if a profile could be described by a finite Fourier series. The mathematical analysis, however, becomes progressively more complex as the number of higher-order Fourier components is increased. For the present purpose the surface profile is redefined to include only one additional Fourier component:

$$z = u_1 \sin(gy) + u_2 \sin(2gy). \quad (5)$$

In general, u_2 is much smaller than u_1 . For this profile we obtain

$$J_p(k, u_1)J_0(k, u_2) + \sum_n (-1)^{p-n} J_{p-n}(\alpha_n u_1) J_0(\alpha_n u_2) B_n^* \\ - \sum_n B_n^* J_{p-n}(\beta_n u_1) J_0(\beta_n u_2) \\ + \sum_{s=1}^{\infty} \left[A(p, s) + \sum_n B(p, n, s) + \sum_n C(p, n, s) \right] = 0 \quad (6)$$

and

$$D(p) + \sum_n E(p, n) - \frac{1}{\epsilon} \sum_n F(p, n) \\ + \sum_{s=1}^{\infty} \left[G(p, s) + \sum_n I(p, n, s) - \frac{1}{\epsilon} \sum_n L(p, n, s) \right] = 0, \quad (7)$$

where A, B, C, D, E, F, G, I , and L are defined in Appendix A.

Equations (6) and (7) reduce to Eqs. (3) and (4) for $u_2 = 0$. The terms in these equations are of the general form $J_s J_p$; in the numerical calculations terms are retained up to $s + s' = 3$; i.e., $J_0 J_0, J_0 J_1, J_0 J_2, J_0 J_3, J_1 J_1$, and $J_1 J_2$.

8. COMPARISON BETWEEN THEORY AND EXPERIMENT

In a previous analysis of first-order coupling to SPW's it was shown that the best fit to the experimental results was obtained for a Ag-film dielectric constant of $(-13.65, 0.82)$ (Ref. 5); this value was used without further adjustment. In Fig. 16 experimental and theoretical reflectance scans versus angle are shown for an 854-nm-period grating with a nearly sinusoidal profile. The theoretical calculations were carried out with the use of Eqs. (6) and (7). Note that the calculated $+1$ -order coupling resonance line shape in the -1 -diffraction-order scan (Fig. 16b) is similar to the 0-order line shape (Fig. 16a) and that the two resonances are comparable, although only a small enhancement rather than a coupling dip at the -2 -order resonance is observed in the 0-order scan. The theoretical line shapes (Figs. 16c and 16d) closely follow the experimental line shapes, although the observed resonance widths are slightly larger than those predicted.

For grating profiles deviating from a sinusoidal shape, u_1 and u_2 were adjusted to produce line shapes closest to those experimentally observed. In Fig. 17 the experimen-

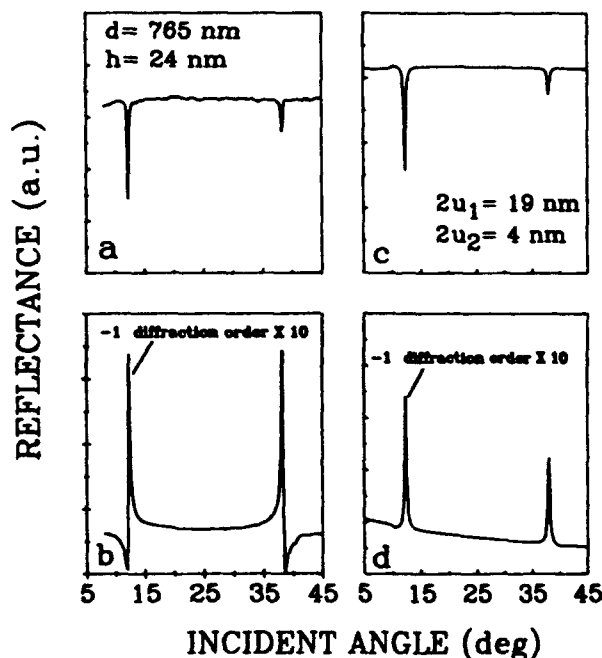


Fig. 17. Comparison between theory and experiment for a profile showing a slight deviation from a sinusoidal shape. The left-hand column presents experimental results; the right-hand column presents theoretical modeling.

tal and calculated plots for a grating with a 765-nm period are shown. This grating deviated from a sinusoidal profile and showed appreciable coupling in the second order (Fig. 17a). In the -1 diffraction order sharp spikes in intensity at SPW resonance minima are observed (Fig. 17b). The calculated 0-order plot (Fig. 17c) is similar to the experimental plot (Fig. 17a). The calculated -1 -diffraction-order plot (Fig. 17d), although showing intensity spikes at both SPW resonances, fails to display the experimentally observed dispersionlike minima, shows unequal intensities at the SPW resonances, and does not replicate the observed diffraction efficiency enhancement in the region between the SPW resonances.

Thus this simple model includes many of the major features observed, but for a complete description higher Fourier coefficients must be included, as we can see in comparing the experimental and theoretical plots in Figs. 3a–3d and 3e–3h above. Note the following features:

- (1) The resonance line shapes in the second order are different (Figs. 3a–3c and 3e–3g),
- (2) The observed grating depths are much larger than those predicted (Figs. 3a–3c and 3e–3g),
- (3) The calculated angular shifts are much smaller than those observed.

The large difference in grating depths and the second-order line shapes is due to the omission of higher Fourier coefficients in the grating profile that result in cancellation effects in second-order coupling. Specifically, the model at present does not include a third-order coefficient. Yet, as we discussed above, it is just this Fourier component of the grating that resonantly couples the counterpropagating SPW modes. For deeper gratings the comparison between observed (Figs. 4a–4d) and predicted (Figs. 4e–4h) reflectance scans show the following features:

- (1) There is an evolution to a broad minimum (Figs. 4e–4h),
- (2) The calculated and observed depths are similar (Figs. 4a–4c and 4e–4g),
- (3) The calculated angular shifts are smaller than those observed,
- (4) The calculated energy coupled to the diffraction order is much higher than that observed.

Note that the calculated plot in Fig. 4h is for a sinusoidal profile, while the actual profile shows considerable deviation from a sinusoidal shape (Fig. 5d). These comparisons emphasize the importance of knowledge of the exact profile for calculation of its reflectance behavior.

The comparison of calculated (Figs. 8a–8d) and observed (Figs. 8e–8h) diffraction-order line shapes shows the following features:

- (1) There is a lack of energy enhancement in the region between intensity spikes (Figs. 8e–8h),
- (2) The calculated spikes in intensity are slightly asymmetric (Figs. 8e–8g),
- (3) The calculated energy in the diffraction order is higher than that observed.

For deeper gratings a similar comparison of observed (Figs. 9a–9d) and calculated (Figs. 9e–9h) diffraction-order line shapes shows the following features:

- (1) An energy enhancement for the calculated line shapes in the region between SPW resonances (Figs. 9e–9h),
- (2) The appearance of shallow minima (Figs. 9e–9h),
- (3) The appearance of an asymmetric line shape in Fig. 9g,
- (4) The sharp decrease in signal from $\sim 10^\circ$ to 15° in Fig. 9h.

Thus the comparison of theory and experimental results indicates that, although the theory manages to show major features of our data, many finer details are not observed. A more detailed theoretical investigation, including both higher Fourier coefficients and a more rigorous formalism, is necessary to provide a detailed fit between theory and experiment.

9. SUMMARY

A systematic experimental study of interactions between SPW couplings in the $(+1, -2)$ minigap regions is reported. The experiment covers the entire range of SPW interactions, ranging from weak-coupling to stronger-coupling effects and to deeper profiles showing absorption rather than SPW effects. The simple theoretical model, although missing many of the finer details, shows the major features of our experimental data. One can develop a better model by including several Fourier coefficients in the grating profile.

Several extensions of this work are immediately apparent. For larger grating periods there are more diffraction orders, and it would be interesting to see how energy is distributed in these orders at SPW resonance angles. Also, the appearance of momentum gaps in the 0 order depends on the strength of interactions.

As we noted above, there has been much discussion of the physical significance of momentum and energy gaps in the minigap regions. As this study, as well as others,^{10,11,14} demonstrated, the response surface is quite complex in the vicinity of a minigap, and a complete analysis of the experimental situation is necessary. Most theoretical treatments of SPW effects on gratings can be cast as a linear algebraic problem of the general form $\mathbf{M}\mathbf{E} = \mathbf{S}$, where the vector \mathbf{E} represents the response fields, \mathbf{M} is the medium response matrix, and \mathbf{S} is the source of excitation vector. Formally, this is solved as $\mathbf{E} = \mathbf{M}^{-1}\mathbf{S}$, where each term in the inverse matrix is proportional to $(\det \mathbf{M})^{-1}$. In many situations knowledge of this determinant, and hence of the dispersion relation, is sufficient for an understanding of the main features of the response. For example, for the case of a single SPW resonance, the experimental dispersion relation obtained from the resonance angles and the linewidths of the 0-order coupling dips are in reasonable agreement with that calculated from the determinant of \mathbf{M} ; higher-order terms can be added to evaluate the effect of deeper gratings.⁶ In the minigap region this procedure clearly is not appropriate; for example, neither of the extrema observed in the first-order coupling coincides with the 0-order coupling resonance angles. In this situation it is not possible simply to extract a dispersion relation from the experimentally observed line shapes. A full treatment of the system response is necessary for interpretation of the measurements in terms of modes and dispersion relations.

APPENDIX A

For a TM-polarized plane wave incident on a sinusoidal interface we can define a (magnetic) B field below and above the grating by using the Rayleigh hypothesis:

$$B^-(y, z) = \exp[i(k_y y + k_z z)] + \sum_n B_n^- \exp[i(K_n y - \alpha_n z)], \quad z < 0,$$

$$B^+(y, z) = \sum_n B_n^+ \exp[i(K_n y + \beta_n z)], \quad z > 0,$$

where $k_y = k_0 \sin \theta$, $k_z = k_0 \cos \theta$, $k_0 = \omega/c$, $k_n = k_y + n g$ ($n = 0, \pm 1, \pm 2$), $g = 2\pi/d$ (d is the grating period), and

$$\alpha_n = i(k_n^2 - k_0^2)^{1/2}, \quad \beta_n = i(k_n^2 - \epsilon k_0^2)^{1/2}.$$

For a sinusoidal surface the profile is given by

$$f(y) = u \sin(gy),$$

so that, by applying the generating function for Bessel functions, we obtain

$$\exp[i\gamma f(y)] = \exp[i\gamma u \sin(gy)] = \sum_{p=-\infty}^{\infty} \exp(ipgy) J_p(\gamma u).$$

By applying the boundary conditions

$$B^-(y, z) = B^+(y, z)|_{z=f(y)},$$

$$\frac{\partial}{\partial n} B^-(y, z) = \frac{1}{\epsilon} \frac{\partial}{\partial n} B^+(y, z)|_{z=f(y)},$$

where $\partial/\partial n$ is the normal derivative to the surface and is defined by

$$\frac{\partial}{\partial n} = \left\{ 1 + \left[\frac{\partial f(y)}{\partial y} \right]^2 \right\}^{-1/2} \left[\frac{\partial}{\partial z} - \frac{\partial f(y)}{\partial y} \frac{\partial}{\partial y} \right],$$

we arrive at Eqs. (3) and (4) above. For a more complex sinusoidal surface the profile is given by

$$f(y) = u_1 \sin(gy) + u_2 \sin(2gy),$$

and we obtain

$$\exp[i\gamma f(y)] = \sum_{p,q} \exp[i(p+2q)gy] J_p(\gamma u_1) J_q(\gamma u_2).$$

Again, applying the boundary conditions leads to Eqs. (6) and (7) above, where the constants are given by

$$A(p, s) = [J_{p-2s}(k_s u_1) + (-1)^s J_{p+2s}(k_s u_1)] J_s(k_s u_2),$$

$$B(p, n, s) = (-1)^{p-n} B_n^- [J_{p-n-2s}(\alpha_n u_1) + (-1)^s J_{p-n+2s}(\alpha_n u_1)] J_s(\alpha_n u_2),$$

$$C(p, n, s) = B_n^+ [J_{p-n-2s}(\beta_n u_1) + (-1)^s J_{p-n+2s}(\beta_n u_1)] J_s(\beta_n u_2),$$

$$D(p) = [K_s - pg(k_y/k_s)] J_p(k_s u_1) J_0(k_s u_2) - g k_s u_2 \times [J_{p-2}(k_s u_1) + J_{p+2}(k_s u_1)] J_0(k_s u_2),$$

$$E(p, n) = -(-1)^{p-n} B_n^- [\alpha_n - (p-n)g(k_n/\alpha_n)] \times J_{p-n}(\alpha_n u_1) J_0(\alpha_n u_2) - g k_n u_2 B_n^+ \times [J_{p-n-2}(\alpha_n u_1) + J_{p-n+2}(\alpha_n u_1)] J_0(\alpha_n u_2),$$

$$F(p, n) = B_n^+ [\beta_n - (p-n)g(k_n/\beta_n)] \times J_{p-n}(\beta_n u_1) J_0(\beta_n u_2) - g k_n u_2 B_n^- \times [J_{p-n-2}(\beta_n u_1) + J_{p-n+2}(\beta_n u_1)] J_0(\beta_n u_2),$$

$$G(p, s) = [k_s - (p-2s)g(k_s/k_s)] J_{p-2s}(k_s u_1) J_s(k_s u_2) + (-1)^s [k_s - (p+2s)g(k_s/k_s)] J_{p+2s}(k_s u_1) \times J_s(k_s u_2) - g k_s u_2 [J_{p-2s-2}(k_s u_1) + (-1)^s J_{p+2s-2}(k_s u_1)] J_s(k_s u_2) - g k_s u_2 \times [J_{p-2s+2}(k_s u_1) + (-1)^s J_{p+2s+2}(k_s u_1)] J_s(k_s u_2),$$

$$I(p, n, s) = -(-1)^{p-n} B_n^- [\alpha_n - (p-n-2s)g(k_n/\alpha_n)] \times J_{p-n-2s}(\alpha_n u_1) J_s(\alpha_n u_2) + (-1)^s B_n^+ \times [\alpha_n - (p-n+2s)g(k_n/\alpha_n)] \times J_{p-n+2s}(\alpha_n u_1) J_s(\alpha_n u_2) - g k_n u_2 B_n^- \times [J_{p-n-2s-2}(\alpha_n u_1) + (-1)^s J_{p-n+2s-2}(\alpha_n u_1)] \times J_s(\alpha_n u_2) - g k_n u_2 B_n^+ [J_{p-n+2s+2}(\alpha_n u_1) + (+1)^s J_{p-n-2s+2}(\alpha_n u_1)] J_s(\alpha_n u_2),$$

$$L(p, n, s) = B_n^+ [\beta_n - (p-n-2s)g(k_n/\beta_n)] \times J_{p-n-2s}(\beta_n u_1) J_s(\beta_n u_2) + (-1)^s B_n^- \times [\beta_n - (p-n+2s)g(k_n/\beta_n)] \times J_{p-n+2s}(\beta_n u_1) J_s(\beta_n u_2) - g k_n u_2 B_n^- \times [J_{p-n-2s-2}(\beta_n u_1) + (-1)^s J_{p-n+2s-2}(\beta_n u_1)] \times J_s(\beta_n u_2) - g k_n u_2 B_n^+ [J_{p-n+2s+2}(\beta_n u_1) + (-1)^s J_{p-n-2s+2}(\beta_n u_1)] J_s(\beta_n u_2).$$

ACKNOWLEDGMENTS

This work was partially supported by the U.S. Air Force Office of Scientific Research. We appreciate the assistance of Anadi Mukherjee and An-Shiang Chu in the tunable laser measurements.

M. Yousaf is also with the Department of Physics and Astronomy, University of New Mexico, Albuquerque, New Mexico 87131. S. R. J. Brueck is also with the Department of Electrical and Computer Engineering and the Department of Physics and Astronomy, University of New Mexico, Albuquerque, New Mexico 87131.

*Present address, Electronics Division, PINSTECH, P.O. Box Nilore, Islamabad, Pakistan.

REFERENCES

1. R. M. Wood, *Phys. Rev.* **48**, 928 (1935).
2. U. Fano, *J. Opt. Soc. Am.* **31**, 213 (1941).
3. R. Petit, ed., *Electromagnetic Theory of Gratings* (Springer-Verlag, Berlin, 1980).
4. V. M. Agranovich and D. L. Mills, eds., *Surface Polaritons* (North-Holland, Amsterdam, 1982).
5. S. H. Zaidi, M. Yousaf, and S. R. J. Brueck, *J. Opt. Soc. Am. B* **8**, 770 (1991).
6. J. E. Stewart and W. S. Gallaway, *Appl. Opt.* **1**, 421 (1962).
7. R. H. Ritchie, E. T. Arakawa, J. J. Cowan, and R. N. Hamm, *Phys. Rev. Lett.* **31**, 1630 (1968).
8. M. C. Hutley, *Opt. Acta* **20**, 607 (1973).
9. M. C. Hutley and V. M. Bird, *Opt. Acta* **20**, 771 (1973).
10. N. Kroo, Z. S. Szentirmay, and J. Felzerfalvi, *Phys. Lett. A* **86**, 445 (1981).
11. Y. J. Chen, E. S. Koteles, R. J. Seymour, G. J. Sonek, and J. M. Ballantyne, *Solid State Commun.* **48**, 95 (1983).
12. M. G. Weber and D. L. Mills, *Phys. Rev. B* **34**, 2893 (1986).

13. P. Tran, V. Celli, and A. A. Maradudin, *Opt. Lett.* **13**, 530 (1988).
14. D. Heitman, N. Kroo, C. Schulz, and Zs. Szentirmay, *Phys. Rev. B* **35**, 2660 (1987).
15. D. Heitman, *Opt. Commun.* **30**, 292 (1977).
16. W. Rothballer, *Opt. Commun.* **30**, 429 (1977).
17. E. H. Rosengart and I. Pockrand, *Opt. Lett.* **1**, 194 (1977).
18. E. A. Stern, as quoted in R. A. Ferrel, *Phys. Rev.* **111**, 1214 (1958).
19. S. H. Zaidi and S. R. J. Brueck, *Appl. Opt.* **27**, 2999 (1988).
20. R. Petit and M. Cadilhac, *C. R. Acad. Sci.* **259**, 2077 (1964).
21. A. Wirgin, *Rev. Opt.* **9**, 449 (1964).
22. J. L. Uretaki, *Ann. Phys.* **33**, 400 (1965).
23. N. E. Glass, M. Weber, and D. L. Mills, *Phys. Rev. B* **29**, 6548 (1984).
24. B. Laks, D. L. Mills, and A. A. Maradudin, *Phys. Rev. B* **23**, 4965 (1981).
25. K. Utagawa, *J. Opt. Soc. Am.* **69**, 333 (1979).
26. M. Nevière, P. Vincent, and R. Petit, *Nouv. Rev. Opt.* **5**, 6577 (1974).
27. H. Numata, *J. Phys. Soc. Jpn.* **51**, 2575 (1982).
28. M. Yamashita and M. Tsuji, *J. Phys. Soc. Jpn.* **52**, 2462 (1983).
29. M. G. Weber, *Phys. Rev. B* **33**, 909 (1986).
30. P. M. Van den Berg and J. J. Fokkema, *J. Opt. Soc. Am.* **69**, 27 (1979).